Summer 7-1-1992

Microstrip Patch Antenna Configurations Suitable for Integration in Monolithic and Hybrid Microwave Circuits

Rajan Parrikar
University of Colorado Boulder

K C. Gupta
University of Colorado Boulder

MIMICAD TECHNICAL REPORT NO. 14

Microstrip Patch Antenna Configurations Suitable for Integration in Monolithic and Hybrid Microwave Circuits

by

Rajan Parrikar
K.C. Gupta

Department of Electrical and Computer Engineering
University of Colorado
Boulder, Colorado 80309-0425

July 1992

ABSTRACT

This report presents a model for analysis and design of two-layer microstrip patch antenna structures suitable for integration with microwave integrated circuits. Configurations suitable for both monolithic and hybrid circuits are proposed. The Multiport Network Model (MNM) approach is used to transform an electromagnetic field problem into a circuit problem. This method is relatively simple in its implementation and is computationally less expensive than full-wave methods. The radiating structure is represented by three sub-networks which are the Patch Network, the Edge-Admittance Network and the Feed Network. These sub-networks are combined by using the segmentation method to yield an overall equivalent network of the antenna. Sample results of the input impedance of some integrated antenna structures are presented and compared with the results obtained by using the full-wave analysis numerical code PMESH.

ACKNOWLEDGEMENTS

The work presented in this report has been supported by the Center for Microwave-Millimeter Wave Computer-Aided Design (MIMICAD) at the University of Colorado at Boulder as a part of the Project No. 89-2, during the period 1989-1991.

Some of the software used in this research was developed by Dr. Abdelaziz Benalla and made available for this project; we thank him for the same. We also thank Dr. John Moore for his assistance in PMESH simulations.

CONTENTS

CHAPTER 1

INTRODUCTION

The advent of sophisticated printed circuit techniques in recent years has spawned several new circuit and antenna configurations in the area of microwave technology. One such advance has been the development of microstrip patch antennas. In essence, microstrip patch antennas comprise metallic patches printed on a dielectric substrate backed by a ground plane. A simple configuration is depicted in Figure 1.1.

These antennas, which are finding increasing use in such diverse applications such as satellite communication, missile telemetry and biomedical radiators among other things, proffer several advantages such as: 1) Low profile and low weight ; 2) Conformability with the profile of the surface on which they are mounted; 3) Integrability with MICs; 4) Circular polarization obtained from a single element alone and 5) Lost -cost.

In the current microwave design practice, circuit functions and antenna elements are designed separately and then fabricated (frequently) on the same substrate. In the research reported here, we have extended the circuit-antenna integration by proposing that the circuit and antenna functions be designed and integrated together functionally. To that end, we have suggested two-level configurations where circuit functions are realized on the lower substrate and the radiating patches are fabricated on the upper substrate. We expect these two-level configurations to provide the best surface real estate usage by allowing the designer to optimize substrate requirements for both circuit and antenna functions.

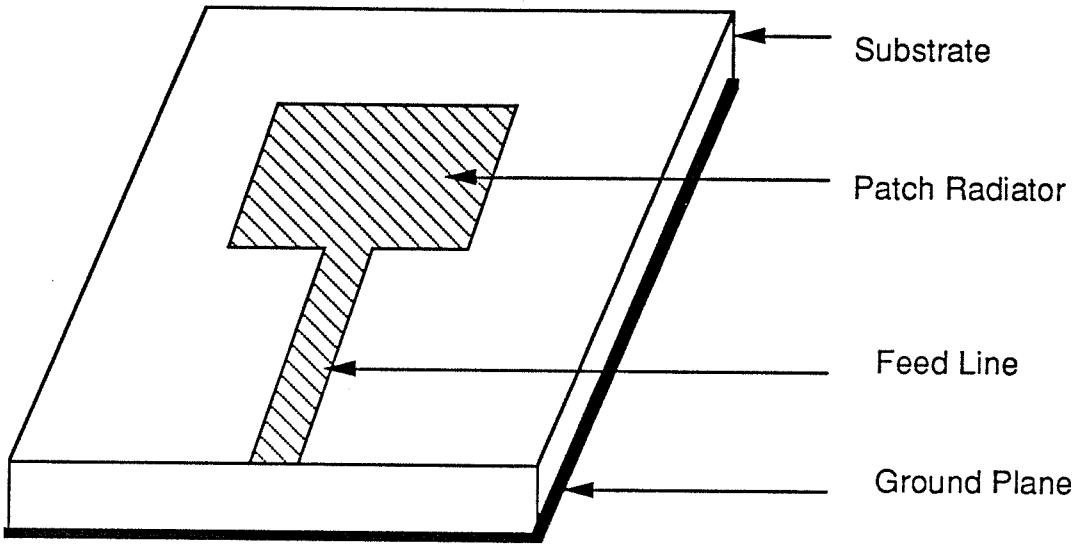

Figure 1.1: Microstrip Patch Antenna fed by a microstrip line

There are three basic mechanisms of exciting a microstrip patch antenna [1]. In the first scheme, the patch is excited by a microstrip line (shown in Figure 1.1). The second method of excitation, shown in Figure 1.2, uses a coaxial line wherein the inner conductor is connected to the patch. The third mechanism for patch excitation uses electromagnetic coupling; here, there is no physical contact between the patch and the feed structure. The patch antenna configurations discussed in this report make use of the excitation mechanism of the third type.

The goal of this research has been to develop a model of two-level radiating configurations wherein the patch resides on the upper substrate and the feed circuitry is located underneath the patch on the lower layer. The excitation of the radiating patch occurs due to electromagnetic coupling between it and the feed network . Two types of configurations are proposed, suitable for monolithic and hybrid integrations, respectively.

Such structures have been the subject of recent investigations [2-5]. However, no design rules exist thus far and the research reported here provides the means for developing a design methodology.

In the monolithic type, shown in Figure 1.3, the lower layer is Gallium Arsenide (GaAs) with a dielectric constant of 12.9 and the upper layer is the thin passivating layer, typically Silicon Nitride with a dielectric constant of 7. The height of the passivating layer is very small (1-2 μm) compared to the GaAs substrate (100-150 μm).

In Figure 1.4, a configuration suitable for hybrid integration is shown. Here, the thickness of the lower layer is much smaller than the upper layer. Also, the lower layer has a dielectric constant which is higher than the upper layer. This being the case, it becomes possible to design a feeder patch on the lower substrate such that it is resonant at approximately the same frequency

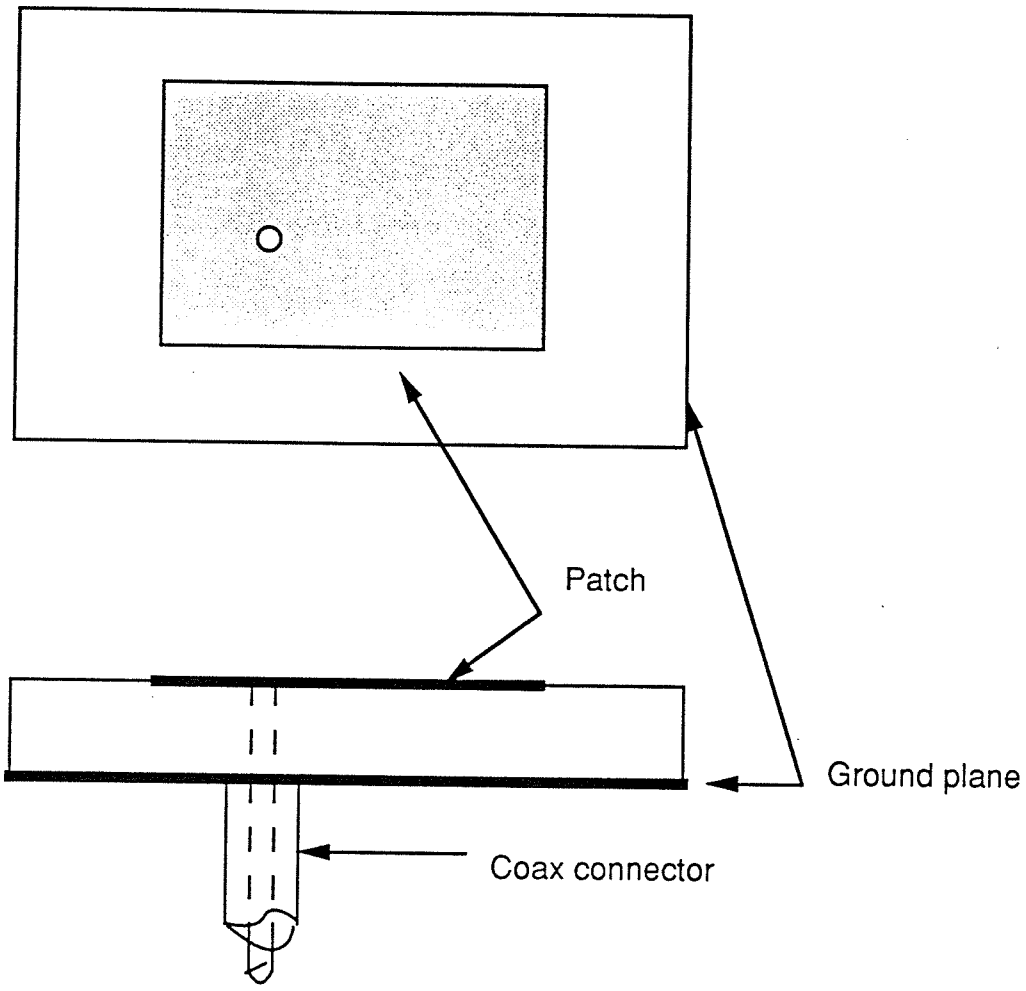

Figure 1.2: Top and Side Views of a Microstrip Patch Antenna fed by a coaxial line

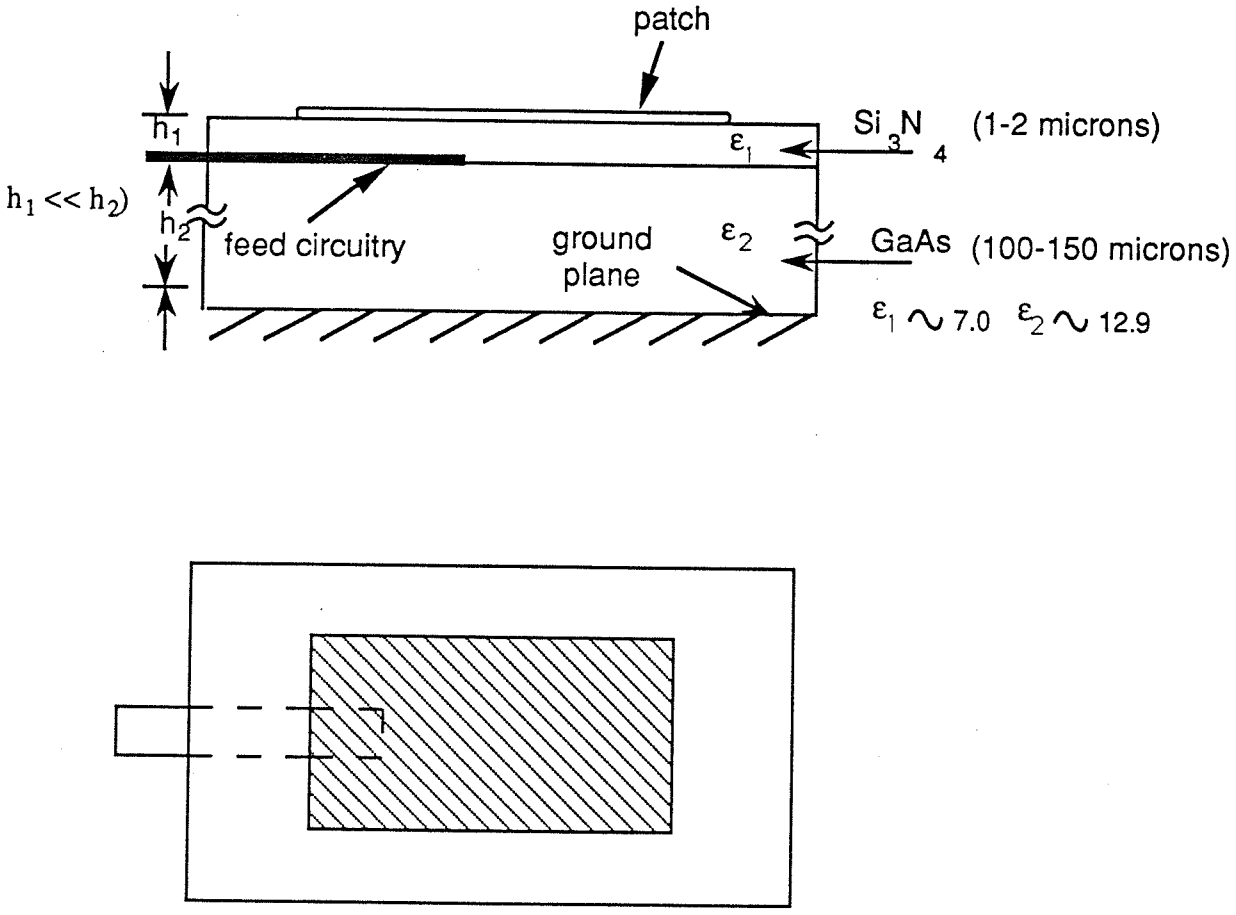

Figure 1.3: A monolithic configuration of a Microstrip Patch Antenna excited by feedline on the lower layer

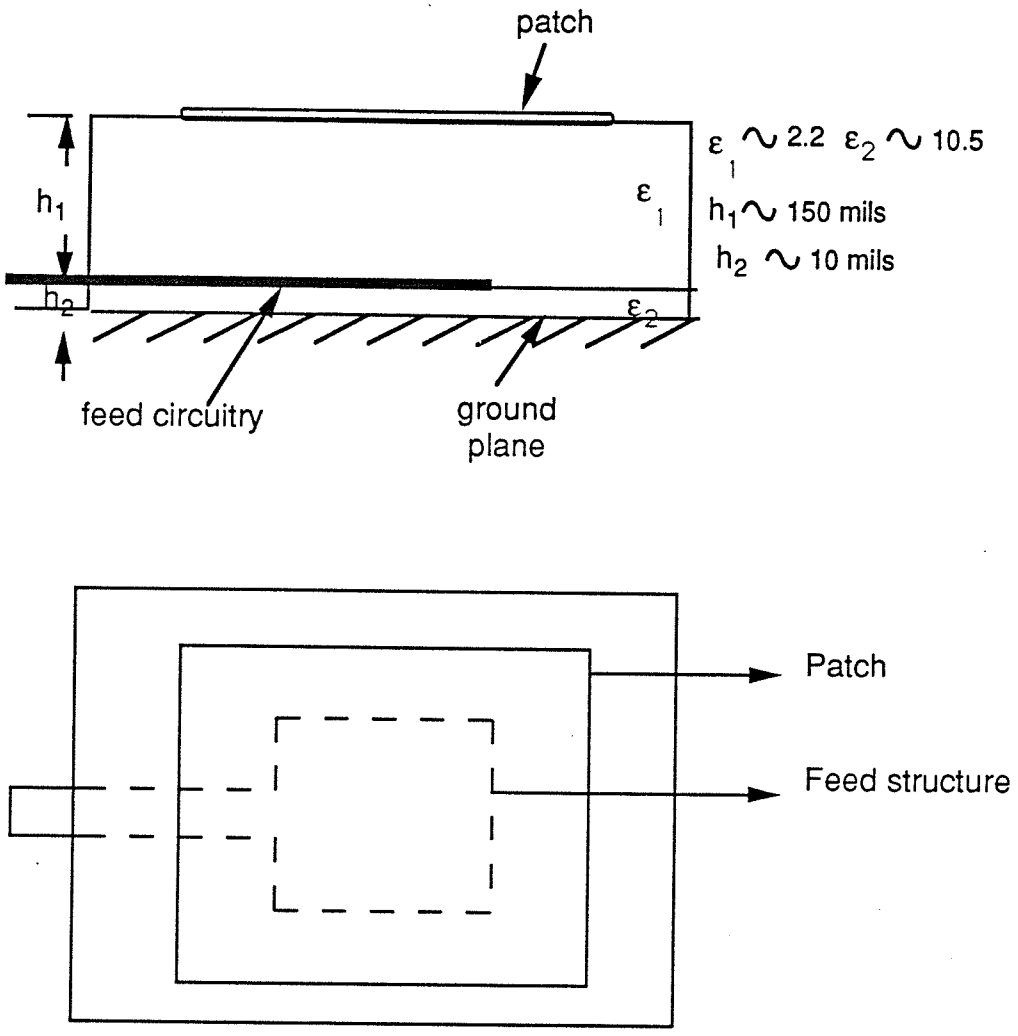

Figure 1.4: Hybrid configuration of a Microstrip Patch Antenna excited by a feeder patch on the lower layer

as the radiating patch. This arrangement is expected to produce a broad-band antenna [1].

In this project, we have developed a model that lends itself for analysis and design of the type of structures shown in Figures 1.3 and 1.4. This model is based on the Multiport Network Model (MNM) for microstrip patch antennas which has been developed at the University of Colorado at Boulder by Gupta and Benalla [6], [7]. The MNM is ideally suited for computer-aided design. It is relatively easy to implement, provides considerable physical insight into the radiation mechanism and it is computationally far less intensive than existing full-wave analysis methods.

Hitherto, the MNM has been used for the analysis and design of single layer patch antennas taking into account only the two-dimensional variation of fields underneath the patch. In our work, we have extended the MNM to analyze two-layered structures and we have also incorporated the three-dimensional variations of the fields underneath the patch. Details of the MNM model are given the Chapters 2 and 3. The the basic idea is that the radiating structure is separated into three regions, each represented by an equivalent sub-network. The three regions are: 1) The region underneath the patch; 2) The region of the fields associated with the feed structure and 3) The region external to the patch which accounts for the radiated power and surface-wave losses. Each of these three regions are modeled separately and a Z-matrix representation for each sub-networkis obtained. Then, the three networks are combined together by a method known as segmentation [8] and the overall network of the radiating structure is realized to yield the input impedance of the antenna and its radiation pattern.

In Chapter 2, the MNM is described in detail. The three sub-networks mentioned earlier are called the Patch Network (PAN), the Feed Network (FN)

and the Edge-Admittance Network (EAN) and procedures for their characterization are detailed.

Chapter 3 deals with the field analysis of the cavity modes. Expressions for obtaining the PAN are developed. Also, expressions for calculating the radiation pattern are given.

Samples results obtained by the MNM method are presented in Chapter 4 and comparison with the full-wave analysis code PMESH is shown.

In Chapter 5, an overview of the completed work is given. A discussion of the approximations in the current MNM model as well as possible ways of refining the model are outlined.

CHAPTER 2

MULTIPORT NETWORK MODEL FOR ELECTROMAGNETICALLY FED PATCH ANTENNAS

The Multiport Network Model (MNM) is an extension of the cavity model [6] and has been used extensively by Gupta and Benalla [7], [9] to evaluate the performance and characteristics of single layer microstrip patches and arrays fed at the edges of the patch. The underlying idea in this approach is that the antenna configuration can be modeled by three (or more) interconnected multiport components. These components represent the fields associated with different regions of the antenna system. Each of these components is characterized as a multiport network and they are combined to yield an overall network model of the radiating system. Using this model, we can compute characteristics such as the input impedance and radiation pattern of the antenna. The three main components of the Multiport Network Model as extended to electromagnetically fed patches are discussed below.

2.1 The Patch Network (PAN)

The PAN models the electromagnetic fields underneath the radiating patch. The external ports of this network are located on the radiating edges of the patch and on the interface to the feed structure underneath the patch as shown in Figure 2.1. The region underneath the patch is essentially viewed as an open cavity and the field distribution is expressed as a summation of electromagnetic cavity modes. This open cavity is surrounded by perfect magnetic walls (zero tangential magnetic field) on the sides and perfect electric walls (zero tangential electric field) on the top and bottom as shown in Figure 2.2. The radiating configuration is excited by a feed structure (usually in the form of a metallic strip) underneath the patch at the

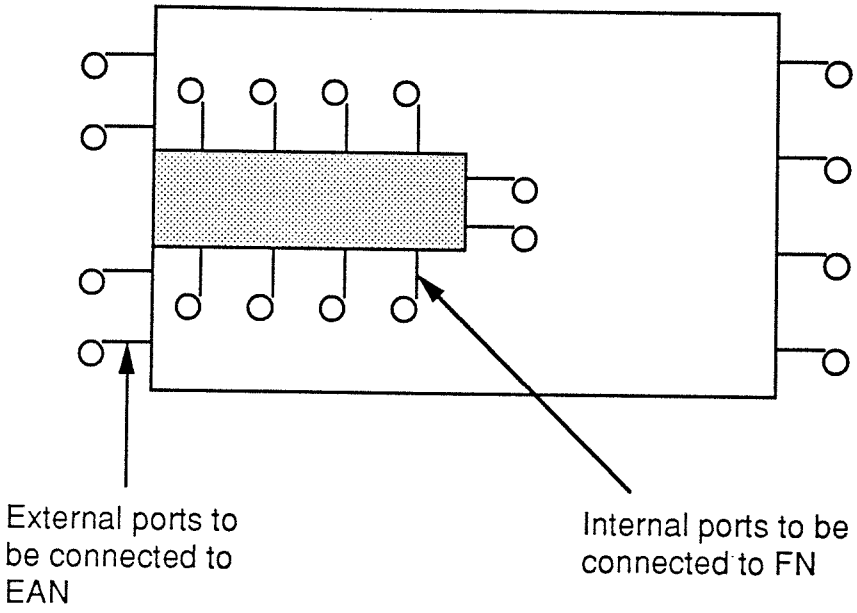

Figure 2.1: Arrangement of ports of the PAN

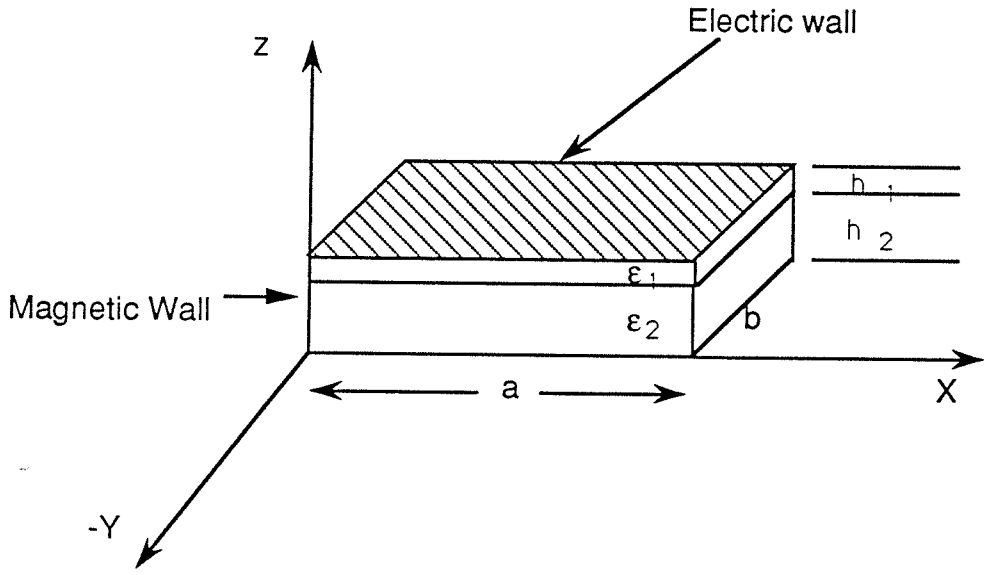

Figure 2.2: Three-dimensional cavity model of the radiating element

interface of the two layers of the substrate. Thus, the source of patch excitation may be represented as an equivalent magnetic current evaluated from the fringing electric field at the edges of the feed structure. These equivalent magnetic currents placed at the periphery of the feed structure are shown in Figure 2.3. Therefore, the fields in the region underneath the patch, which has been considered as an open cavity, are produced by these equivalent magnetic current elements.

The major contribution to the radiation from a patch, excited at a frequency in the vicinity of the dominant resonance frequency, comes from the radiating edges. The radiation from the non-radiating edges is relatively small and contributes to the cross-pol [6] and hence is not considered in the computations presented in this report. The radiating edges of the patch are sub-divided into small sections, each represented by a network port. The voltages at these ports due to excitation by the feed are evaluated by the method presented later.

The substrate of the radiating structure considered is a two-layered one (see Figure 2.2). However, analysis of the two-layer structure is simplified considerably by defining an effective dielectric constant which allows the two-layer cavity to be treated as a homogeneously filled single layer structure as shown in Figure 2.4. Two different methods for obtaining this effective dielectric constant are outlined below.

a) Microstrip patch antennas are usually excited at or near the dominant resonant frequency of one of the cavity modes. The fields for the dominant TM_{10} mode are independent of z and the electric field has only a z-component. In this case, the concept of equivalence of capacitances may be used. The effective dielectric constant thus defined yields the same resonance frequencies as the original two-layer structure. Furthermore, in the configurations investigated in this work, one of the two layers is always much thinner than the other and this effective dielectric constant approximation is fairly accurate for design purposes. A

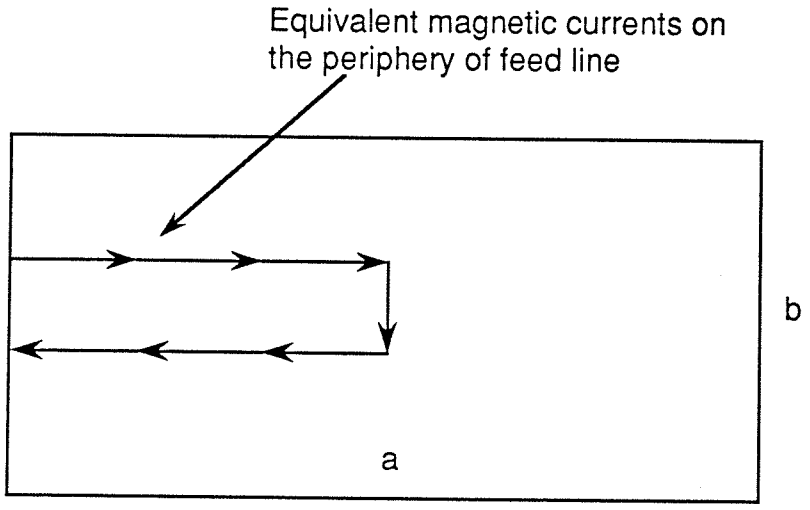

Figure 2.3: Modeling of the feed structure using equivalent magnetic current elements

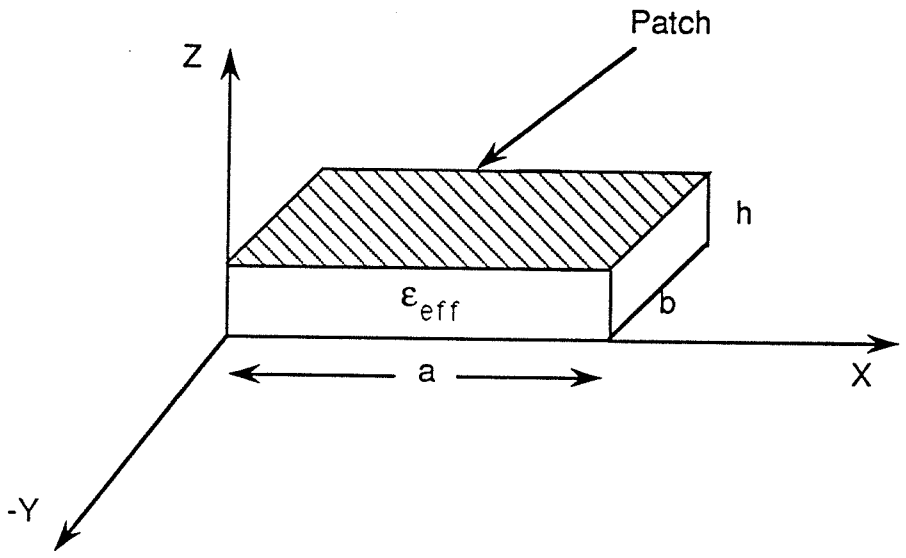

Figure 2.4: Open cavity filled homogeneously with an effective dielectric constant

comparison between the first few dominant resonance frequencies of a two-layer cavity obtained by rigorous two-layer analysis and by the effective dielectric constant method given above is shown in Appendix A.

b) An alternative method for obtaining the effective dielectric constant is based on the quasi-static spectral domain analysis of the two layer transmission line. In this technique, the patch on a multilayered substrate is considered as a transmission line exhibiting the TEM mode of propagation. The Green's function associated with a multilayered substrate is determined and the charge distribution on the metallic portions of the configuration is evaluated by numerically solving Poisson's differential equation to yield the static capacitance [10], [11], [12]. This leads to the determination of the transmission line parameters such as the characteristic impedance and the effective dielectric constant. In our work, we have used this method for obtaining the effective dielectric constant of the PAN. To obtain the effective dielectric constant of the PAN, the patch is viewed as a two-layer microstrip line of width b as shown in Figure 2.5.

The modal analysis of the fields in the cavity leads to an impedance matrix for the Patch Network (PAN). In calculating the impedance matrix for the PAN, an intermediate step is the evaluation of a hybrid matrix, details of which are described in Chapter 3.

2.2 The Feed Network (FN)

The FN models the fields associated with the feed structure situated at the interface of the two layers. Two feed structures which are proposed in this work are: a stripline and a stepped stripline (shown in Figures 2.6a and 2.6b) to provide the impedance match. The corresponding feed network configuration for the arrangement in Figure 2.6a is depicted in Figure 2.7. In hybrid circuit configurations, it is possible to have a resonant feed structure at the interface of the

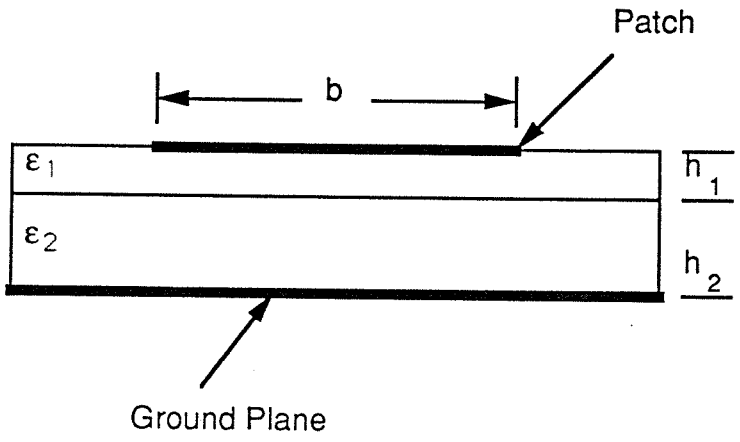

Figure 2.5: The radiating patch considered as a two-layer microstrip line

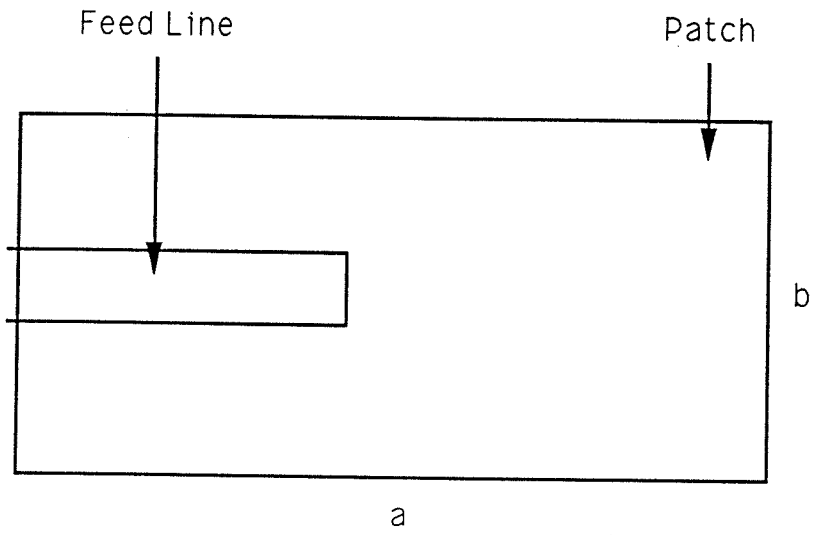

Figure 2.6 a: Radiating Patch Fed by a Line at the Two-Layer Interface

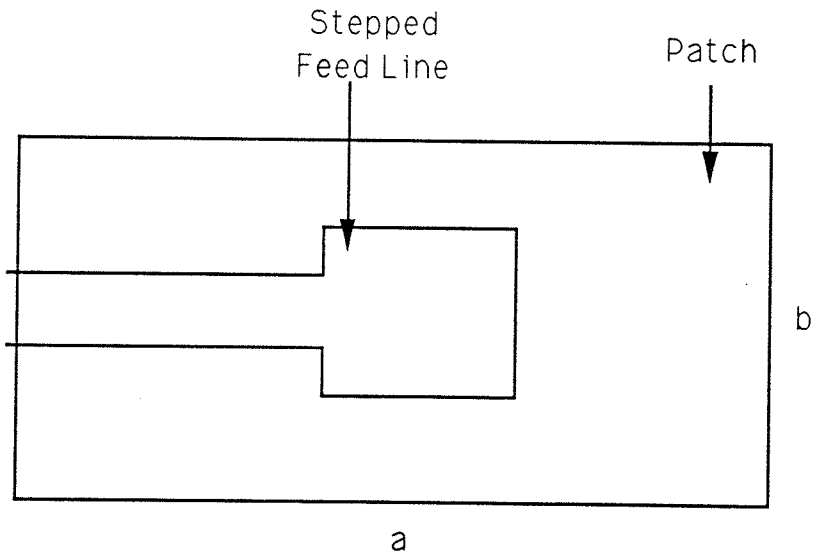

Figure 2.6 b: Radiating Patch Fed by a Stepped Line at the Two-Layer Interface

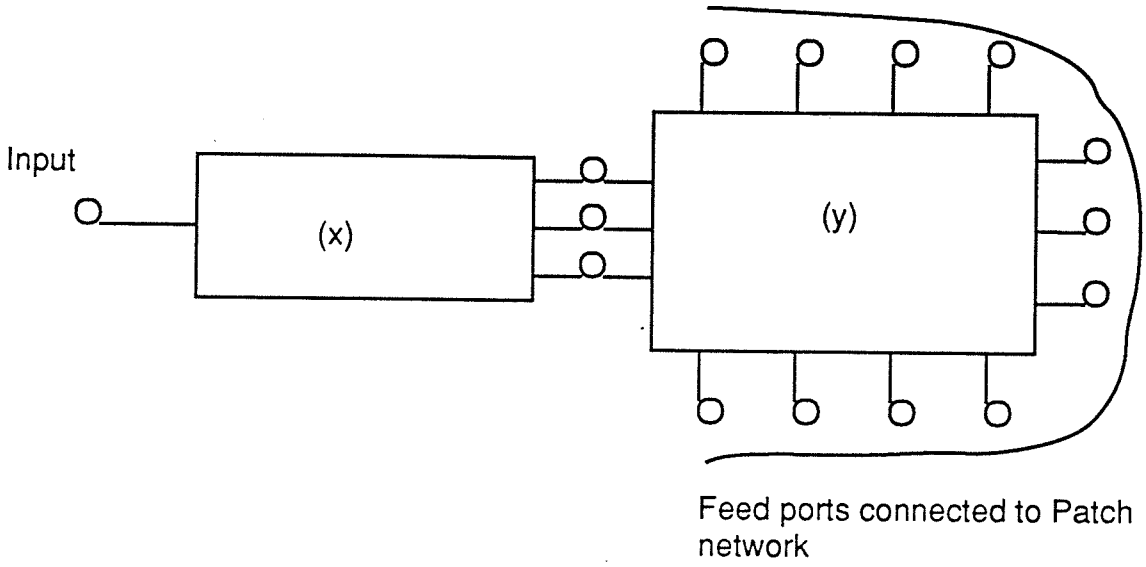

Figure 2.7: Feed network of the configuration in Figure 2.6a. Segment (x) represents a short section of microstrip outside the patch.

two layers since the higher dielectric constant of the lower layer makes the resonant size small enough to be located underneath the patch.

Several other feed circuit configurations (both passive and active) may be located underneath the patch. Some interesting possibilities are mentioned as a part of concluding remarks in Chapter 5.

The feed structure, being very close to the ground plane or the radiating patch (monolithic and hybrid circuits, respectively), essentially supports transmission line modes. Since the width of the feedline is much smaller than that of the patch, we consider the feed configuration to be a two layer asymmetric stripline as shown in Figure 2.8. A planar waveguide model of this line is constructed and two-dimensional planar analysis is used to compute the Z-matrix of the feed structure [13]. A typical feed network will have one port at the input and several output ports which get connected to the input ports of the patch network. It may consist of two or more subnetworks depending upon the layout of the feed configuration.

2.3 The Edge-Admittance Network (EAN)

The edge-admittance network accounts for the fields external to the patch namely, the fringing field, the radiated field and the surface wave fields. This EAN is connected to the edge ports of the PAN. For the results included in this report, the surface wave field has been neglected since its effect for electrically thin substrates is small. An alternative method for modeling the fringing field at the edges of the patch is by extending the physical dimensions of the patch outwards as shown in Figure 2.9. Several empirical formulas are available for calculating the fringing capacitance or the outward extension of physical dimensions of the patch. The expression used here the outward extension of physical dimension is [14]:

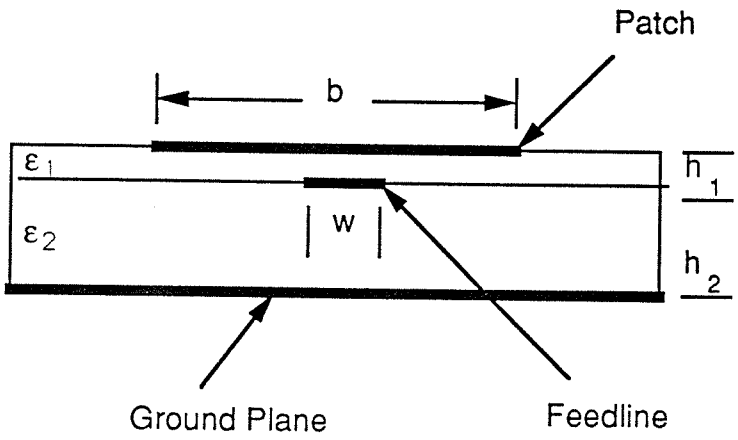

Figure 2.8: The feedline considered as a two-layer asymmetric stripline

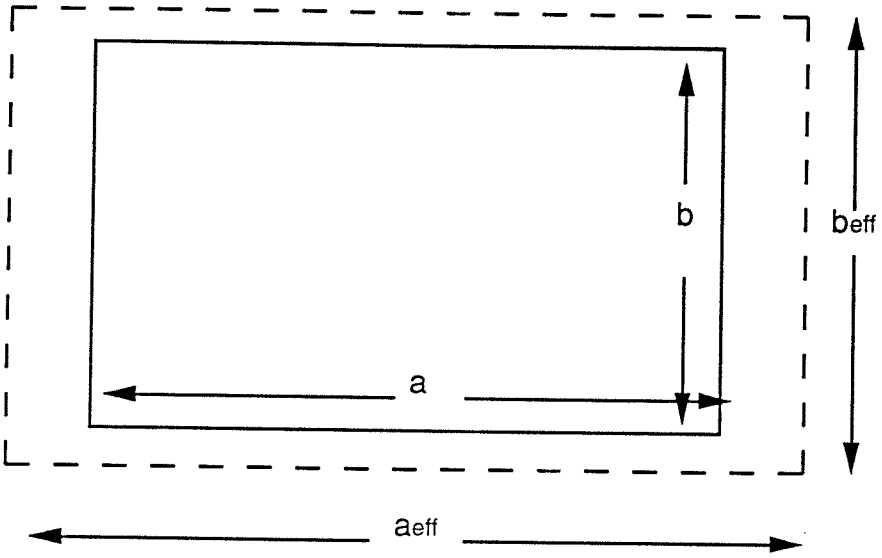

Figure 2.9: Extension of Physical Widths of the Patch to Model Fringing Field

$$\frac{\Delta l}{h} = 0.412 \frac{\varepsilon_{re} + 0.300}{\varepsilon_{re} - 0.258} \cdot \frac{(w/h) + 0.262}{(w/h) + 0.813} \qquad (2.1)$$

where Δl is the increment in the physical width on each edge, w is the width of the patch, h and ε_{re} are the height and dielectric constant, respectively, of the substrate.

The radiated power is accounted for by an equivalent radiation conductance network. The value of this radiation conductance, connected to the edge ports of the PAN, is such that the power dissipated by the conductance (in the network model) is equal to the power radiated by the edge of the antenna. The expressions for radiation conductance per unit length are [1]

$$\begin{aligned} G_r &= w^2 / 90\,\lambda^2 , && w < 0.35\,\lambda \\ G_r &= w / 120\,\lambda - 1 / 60\,\pi^2 , && 0.35\,\lambda < w < 2\lambda \\ G_r &= w / 120\,\lambda , && 2\lambda < w \end{aligned} \qquad (2.2)$$

where w is the width of the radiating edge and λ is the wavelength in free space.

The edge-conductance method mentioned above can be used when the voltage distribution along the radiating edge is known *a priori*. The expressions in equation (2.2) hold for the case when the voltage distribution along the length of the edge is uniform. Since the patch antenna is, in most cases, operated at or close to the dominant resonance frequency, the voltage distribution is known at least approximately. This restriction of knowing the voltage distribution *a priori* has been removed by a recent development of the Generalized Edge-Admittance-Network by Gupta and Benalla [15]. We plan to include this advance in future work.

The EAN for the case when the fringing field capacitances are modeled by outward extensions of the edges is shown in Figure 2.10. Note that no radiation conductances are connected to the 'non-radiating edges' of the patch. This implies that radiation from these 'non-radiating edges' is being ignored. Typically, this radiation is less than -15 dB and adds to the cross pol level for linearly polarized antennas operating in the dominant mode. For more accurate modeling, the radiation conductance network should be added to the non-radiating edges also. In several cases (such as circularly polarized antennas), the radiating and non-radiating edges cannot be identified separately and radiation conductance networks need to be added to all the edges [6].

2.4 The Overall Network

The overall network model of the antenna is obtained by connecting the three networks (FN, PAN and EAN) together as shown in Figure 2.11. The three Z-matrices representing the PAN, FN and EAN are combined using the segmentation method [8]. This procedure results in a Z-matrix (1x1) which is the input impedance of the antenna structure. The segmentation process also yields the voltages at the PAN-EAN connected ports. This voltage distribution is expressed as an equivalent magnetic current distribution which is used for computation of the radiation field. The expressions for the radiation field calculation are given in Chapter 3.

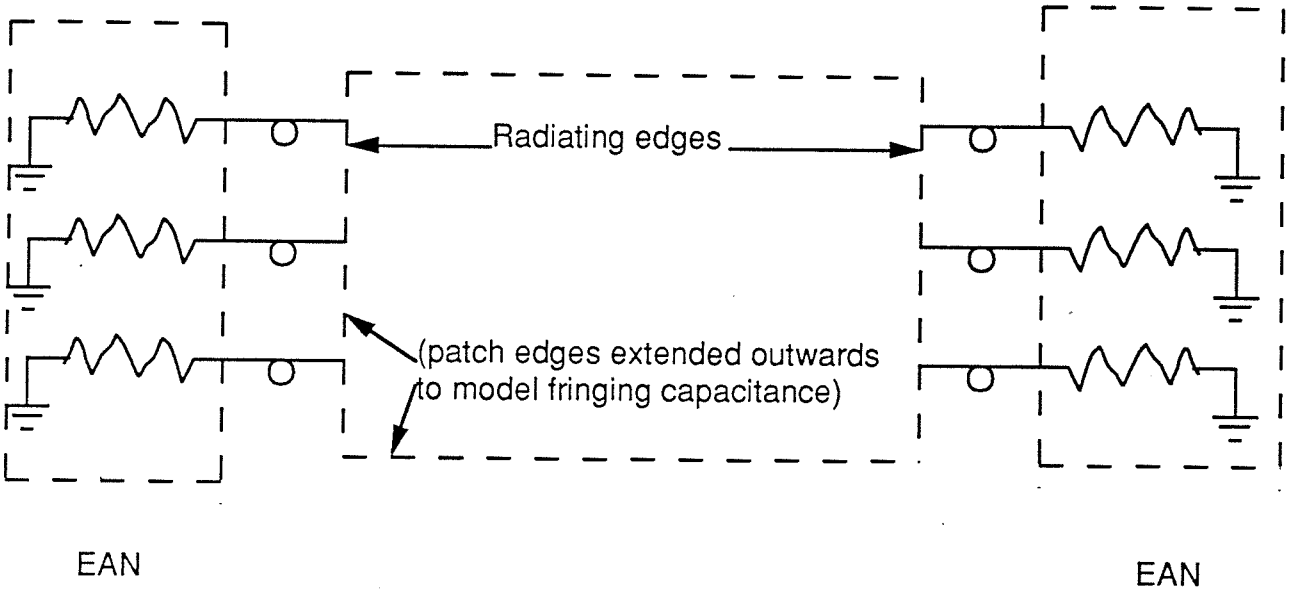

Figure 2.10: Edge-Conductance Network connected to the ports

on the radiating edges

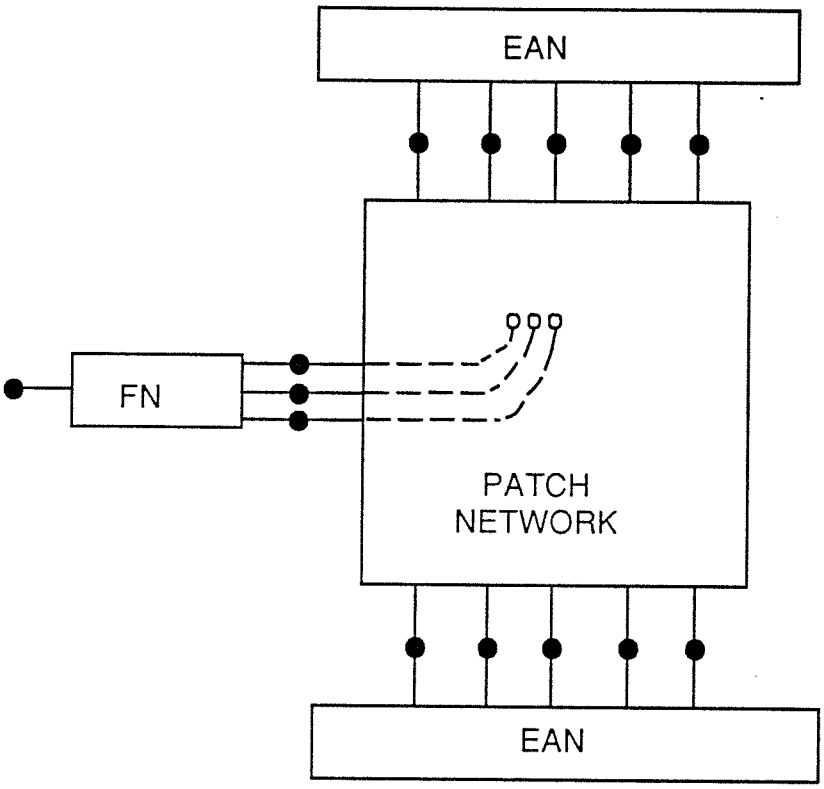

Figure 2.11: Overall Network of the radiating structure

CHAPTER 3

ANALYSIS OF FIELDS ASSOCIATED WITH THE PATCH

This chapter provides an electromagnetic analysis of fields underneath the patch. This leads to the characterization of the PAN described in Chapter 2. The process of segmentation leading to edge voltage calculations and radiation field produced is also discussed.

3.1 Source-free Fields

The original two-layer antenna structure can be analyzed by considering it as a two-layer (inhomogeneous) open cavity. However, this approach entails solving transcendental equations for the resonance frequencies of the cavity modes [16] with concomitant increase in computational effort. As pointed out in Chapter 2, the analysis can be simplified by obtaining an effective dielectric constant (ε_{eff}) to replace the two-layer cavity by a single dielectric layer. The value of ε_{eff} is obtained by using the quasi-static spectral domain technique for the propagation constant of the microstrip line (with width that of the patch) with a two-layer dielectric substrate.

The procedure for determining the fields in the rectangular cavity is on the lines of that given in [17]. The source-free fields in the cavity are expressed as TE or TM to the 'z' coordinate (refer to Figure 2.3). The wave functions must be chosen such that the fields meet the following boundary conditions for the open cavity:

$$\vec{a_n} \times \vec{E} = 0 \text{ on electric walls}$$

$$\vec{a_n} \times \vec{H} = 0 \text{ on magnetic walls} \qquad (3.1)$$

The wave functions of the electric vector potential F_z and the magnetic vector potential A_z, respectively, are thus selected as

$F_z = A_{mnp} \sin \alpha_1 x \sin \alpha_2 y \sin \alpha_3 z$ for TE modes (3.2)

$A_z = B_{mnp} \cos \alpha_1 x \cos \alpha_2 y \cos \alpha_3 z$ for TM modes (3.3)

where $\alpha_1 = m\pi/a$, $\alpha_2 = n\pi/b$ and $\alpha_3 = p\pi/h$. As can be seen, for a non-trivial solution in the TE case, m, n, p = 1, 2, 3, ... while in the TM case, we may have m, n, p = 0, 1, 2, 3, ... When m=n=p=0, the TM mode field corresponds to the static solution.

3.1.1 TE Fields

The electric and magnetic field components for the TE case are obtained [Appendix B] from the wave function given above and are written explicity as follows:

$$E_x = -\frac{\alpha_2}{\varepsilon_1} A_{mnp} \sin\alpha_1 x \cos \alpha_2 y \sin\alpha_3 z$$

$$E_y = -\frac{\alpha_1}{\varepsilon_1} A_{mnp} \cos\alpha_1 x \sin \alpha_2 y \sin\alpha_3 z$$

$$E_z = 0$$

(3.4)

$$H_x = \frac{j \alpha_1 \alpha_3}{\omega_i \mu_0 \varepsilon_1} A_{mnp} \cos\alpha_1 x \sin \alpha_2 y \cos\alpha_3 z$$

$$H_y = \frac{j \alpha_2 \alpha_3}{\omega_i \mu_0 \varepsilon_1} A_{mnp} \sin\alpha_1 x \cos \alpha_2 y \cos\alpha_3 z$$

$$H_z = j\left[\frac{(\alpha_3)^2}{\omega_i \mu_0 \varepsilon_1} - \omega_i\right] A_{mnp} \sin\alpha_1 x \sin\alpha_2 y \sin\alpha_3 z$$

where A_{mnp} is the source-free mode amplitude coefficient and ω_i is the resonance frequency of the ith mode of the TE field (any one combination of m, n and p constitutes the ith mode) given by

$$\omega_i = \{ (\alpha_1)^2 + (\alpha_2)^2 + (\alpha_3)^2 \}^{1/2} \qquad (3.5)$$

3.1.2 TM Fields

The expressions for the TM field components are obtained as:

$$E_x = \frac{j\alpha_1 \alpha_3}{\omega_i \mu_0 \varepsilon_{eff}} B_{mnp} \sin\alpha_1 x \cos\alpha_2 y \sin\alpha_3 z$$

$$E_y = \frac{j\alpha_2 \alpha_3}{\omega_i \mu_0 \varepsilon_{eff}} B_{mnp} \cos\alpha_1 x \sin\alpha_2 y \sin\alpha_3 z$$

$$E_z = j\left(\frac{\alpha_3^2}{\omega_i \mu_0 \varepsilon_{eff}} - \omega_i\right) B_{mnp} \cos\alpha_1 x \cos\alpha_2 y \cos\alpha_3 z \qquad (3.6)$$

$$H_x = -\frac{\alpha_2}{\mu_0} B_{mnp} \cos\alpha_1 x \sin\alpha_2 y \cos\alpha_3 z$$

$$H_y = \frac{\alpha_1}{\mu_0} B_{mnp} \sin\alpha_1 x \cos\alpha_2 y \cos\alpha_3 z$$

$H_z = 0$

where

B_{mnp} is the source-free mode amplitude coefficient for the TM fields and ω_i is the respective mode resonance frequency.

3.2 Modal Amplitude Coefficients

The orthogonality properties [18], [19] of the cavity modes are used to determine the modal amplitude coefficients A_{mnp} and B_{mnp}. The mode amplitude coefficients are fixed by the orthonormalization equation given by

$$\mu_0 \int_v \vec{H_i} \cdot \vec{H_j^*} \, dV = \delta_{ij} \tag{3.7}$$

where '*' denotes the complex conjugate, δ_{ij} is the Kronekar delta and the subscripts i, j refer to the modes. The integration in (3.7) is over the volume of the cavity and it leads to the following expressions:

$$A_{mnp} = \sqrt{\frac{8\,\varepsilon}{\left[(\alpha_1)^2 + (\alpha_2)^2\right] a\, b\, h}} \qquad m, n, p \neq 0 \tag{3.8}$$

($A_{mnp} = 0$ if m=0 or n=0 or p=0)

for TE modes

and

$$B_{mnp} = 2\sqrt{\frac{\mu_0}{\left[(\alpha_1)^2 + (\alpha_2)^2\right] a\, b\, h}} \qquad m\neq 0,\ n\neq 0,\ p=0$$

$$B_{mnp} = \frac{2}{\alpha_1}\sqrt{\frac{\mu_0}{a\,b\,h}} \qquad m\neq 0,\ n=0,\ p\neq 0$$

$$B_{mnp} = \frac{2}{\alpha_2}\sqrt{\frac{\mu_0}{a\,b\,h}} \qquad m=0,\ n\neq 0,\ p\neq 0 \qquad (3.9)$$

$$B_{mnp} = \frac{1}{\alpha_2}\sqrt{\frac{2\,\mu_0}{a\,b\,h}} \qquad m=0,\ n\neq 0,\ p=0$$

$$B_{mnp} = \frac{1}{\alpha_1}\sqrt{\frac{2\,\mu_0}{a\,b\,h}} \qquad m\neq 0,\ n=0,\ p=0$$

($B_{mnp} = 0$ if m=n=0)

for TM modes.

3.3 Fields due to Magnetic Current Excitation

Once the source-free fields are calculated, we evaluate the fields in the cavity due to the presence of sources, which in our case are magnetic current elements. The expressions for the electric and magnetic fields in a cavity excited by a magnetic current element **M** are [16]

$$\vec{E} = \sum_i^{\infty} \frac{j\omega_i \vec{E_i}}{\omega^2 - \omega_i^2} \int_v \vec{M} \cdot \vec{H_i^*}\, dV \qquad (3.10)$$

$$\vec{H} = \sum_i^{\infty} \frac{j\omega \vec{H_i}}{\omega^2 - \omega_i^2} \int_v \vec{M} \cdot \vec{H_i^*}\, dV \qquad (3.11)$$

where ω_i is the resonant frequency of the ith mode and the integration is over the source coordinates (distribution of M). The '*' denotes a complex conjugate of the quantity preceding it.

The above two equations are written in a more compact form as

$$\vec{E} = \sum_i B_{iE} E_i \tag{3.12}$$

and

$$\vec{H} = \sum_i B_{iH} H_i \tag{3.13}$$

where

$$B_{iE} = \frac{j\omega_i}{\omega^2 - \omega_i^2} \int_v \vec{M} \cdot H_i^* \, dV \tag{3.14}$$

and

$$B_{iH} = \frac{j\omega}{\omega^2 - \omega_i^2} \int_v \vec{M} \cdot H_i^* \, dV \tag{3.15}$$

3.3.1 Source Terms

Consider a cavity excited by a magnetic current element M of length dl as shown in Figure 3.1. We may define x and y components of this element as M_x of length dl_x and M_y of length dl_y, respectively. The dot product in the integral in equations (3.14) and (3.15) can be separated explicitly in terms of the x and y components of the magnetic field as

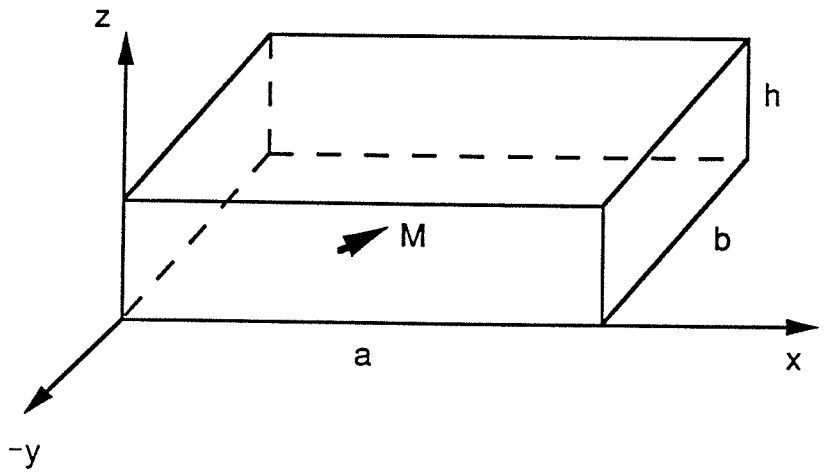

Figure 3.1a: Cavity Excited by Magnetic Current Element of length dl

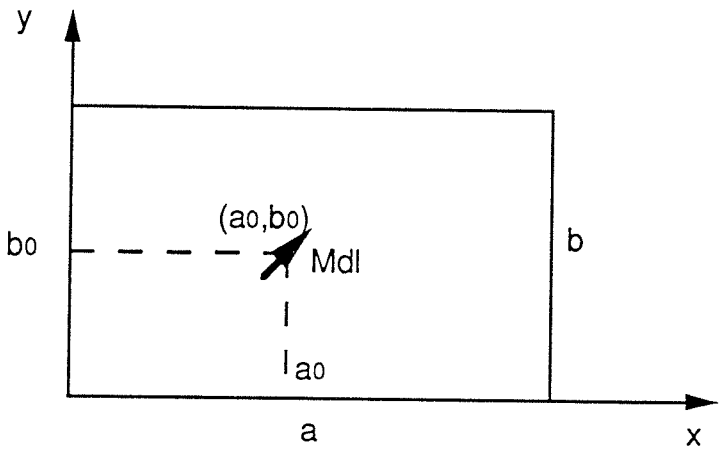

Figure 3.1b: Top view of Figure 6a

$$\int_v \vec{M} \cdot H_i^* \, dV = B_{ix} + B_{iy} \tag{3.16}$$

where

$$B_{ix} = \int_v M_x H_{ix}^* \, dV \tag{3.17}$$

and

$$B_{iy} = \int_v M_y H_{iy}^* \, dV \tag{3.18}$$

Evaluation of the integrals in equations (3.17) and (3.18) yields closed form expressions for the source terms B_{ix} and B_{iy}, viz.,

$$B_{ix} = H_{x0}^* \cos \alpha_1 a_0 \, \sin \frac{\alpha_1 dl_x}{2} \, \sin \alpha_2 b_0 \, \cos \alpha_3 d \tag{3.19}$$

$$B_{iy} = H_{y0}^* \sin \alpha_1 a_0 \, \sin \frac{\alpha_2 dl_y}{2} \, \cos \alpha_2 b_0 \, \cos \alpha_3 d \tag{3.20}$$

where H_{x0}^*, H_{y0}^* denote the complex conjugates of the amplitudes of the respective x and y components of the H-field.

3.4 Voltage at the Edges of the Patch

The expressions developed in the preceding sections are now used to evaluate the voltage at the edge of a radiating patch due to excitation by a magnetic current element in the open cavity (see Figure 3.1).

By definition,

$$v = - \int_0^h \vec{E} \cdot \vec{dl} \tag{3.21}$$

Using equation (3.9), the above equation assumes the form

$$v = -\sum_i B_{iE} \int_0^h \vec{E}_i \cdot \vec{dl} \tag{3.22}$$

Referring to the coordinates in Figure 3.1b, (3.22) reduces to

$$v = -\sum_i B_{iE} \int_0^h \vec{E}_i \cdot \hat{z}\, dz \tag{3.23}$$

The only contribution to the above integral comes from the z-component of the electric field and using the expression for the modal E_z, we have

$$v = -\sum_i B_{iE} \int_0^h E_0 \cos \alpha_1 x \cos \alpha_2 y \cos \alpha_3 z\, dz \tag{3.24}$$

where E_0 is the coefficient of the electric field component E_z.

Since the integration in (3.24) is only over the z-coordinate, the voltage v is equal to zero if α_3 is different from zero. This means that higher order modes involving a variation in the z direction contribute nothing to the voltage. When $\alpha_3 = 0$, the integral reduces to

$$v = -h E_0 \sum_i B_{iE} \cos \alpha_1 x \cos \alpha_2 y \ , \quad p = 0 \tag{3.25}$$

From the expressions for the source terms it is easy to see that dominant mode (m=1, n=0, p=0) can be excited only by a y-directed magnetic current element. Hence, to speed up the computation, ports may be placed only along

the width of the feedline (see Figure 3.3 where ports are placed along the entire periphery of the feedline).

3.5 Equivalent Current over a Port Width

In this section, we use the expressions developed earlier in Section 3.3 to calculate the electric current into (or out of) a port due to a magnetic current element located along the width of the port. This calculation (as well as the ones in Section 3.4) is required to evaluate the hybrid matrix representation (discussed in Section 3.6) for the PAN.

The procedure is described for the cases where the current element is oriented in the y direction (shown in Figure 3.2) and the extension to the case of an arbitrarily oriented current element can be carried out easily. The width of the port is denoted by w and the magnetic current element is centered at (a_0, b_0).

The equivalent linear current density into the width of the port is related to the tangential component of the magnetic field by $\vec{J} = \hat{n} \times \vec{H}$ where $\hat{n}$ is the unit outward normal to the surface. Since the port in Figure 3.2 is oriented in the y direction, the desired component of the above equivalent current into (or out of) the port is J_x. Recognizing that any contribution to J_x comes solely from H_y, the current I is written as

$$I = \int_{b_0-\frac{w}{2}}^{b_0+\frac{w}{2}} \sum_i B_{iH} \vec{H}_i . \hat{y} \, dy \qquad (3.26)$$

The integral is over the port width; using (3.14) and simplifying, results in an expression for the current I given by

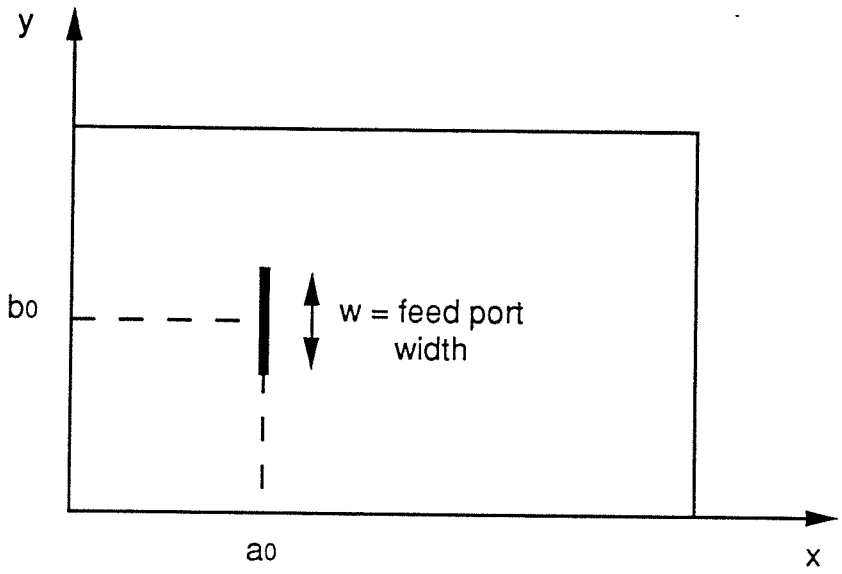

Figure 3.2: Current calculation at feed port

$$I = \sum_i \frac{2 H_0 B_{iH}}{\alpha_2} \sin \alpha_1 a_0 \cos \alpha_2 b_0 \sin \frac{\alpha_2 w}{2} \cos \alpha_3 z \qquad (3.27)$$

Equation (3.27) holds when α_2 is not equal to zero. When $\alpha_2 = 0$, the expression is given by

$$I = \sum_i H_0 B_{iH} w \sin \alpha_1 a_0 \cos \alpha_3 z \ , \ \alpha_2 = 0 \qquad (3.28)$$

H_0 in the last two equations is the coefficient of H_y.

3.6 Hybrid Matrix for PAN

The electromagnetic analysis of the PAN described above yields a hybrid matrix (H-matrix) which is then converted to a Z-matrix characterization.

The first step in this characterization is to place ports on the radiating edges (of width 'b') of the patch and on the feeding microstrip as shown in Figure 3.3. These ports are called edge ports and feed ports respectively. The cavity is excited by magnetic current elements located at the feed port locations. A hybrid matrix relating voltages and currents at the feed and the edge ports is defined by:

$$\begin{bmatrix} \widehat{V_E} \\ \widehat{I_F} \end{bmatrix} = \begin{bmatrix} [H_{11}][H_{12}] \\ [H_{21}][H_{22}] \end{bmatrix} \begin{bmatrix} \widehat{V_F} \\ \widehat{I_E} \end{bmatrix} \qquad (3.29)$$

where

$\widehat{V_E}$ = vector containing the edge port voltages

$\widehat{I_E}$ = vector containing the edge port currents

$\widehat{V_F}$ = vector containing the feed port voltages

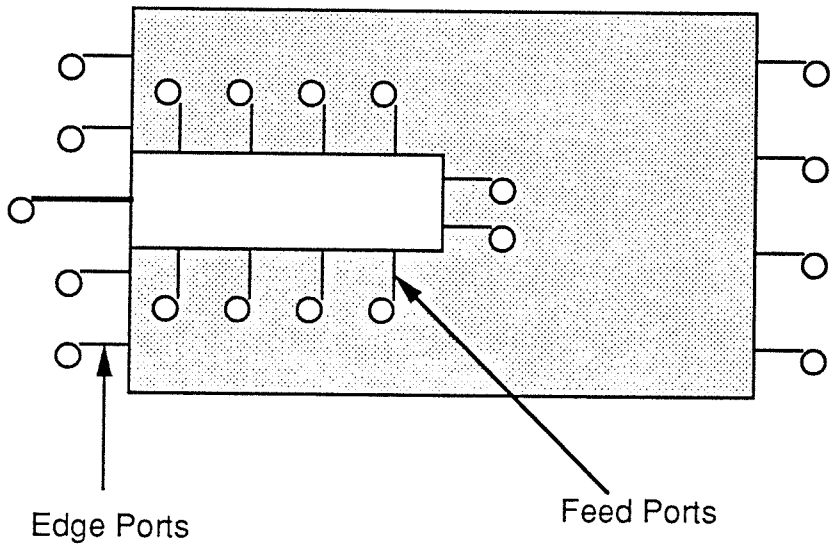

Figure 3.3: Arrangement of patch and feed ports

$\hat{I}_F$ = vector containing the feed port currents

$[H_{11}]$ relates the voltages at the edge ports to the impressed voltages at the feed ports. The expressions for the fields in the cavity derived earlier (equations 3.12 - 3.25) are used to calculate the voltages at the edge ports for a unit magnetic current excitation.

$[H_{12}]$ is the sub-matrix relating the edge port voltages to the edge port currents with the feed ports shorted. When the feed ports are shorted, we are left with a regular patch with no z-varying fields present. This configuration is now a two-dimensional one and the two-dimensional Green's function analysis is used[].

$[H_{21}]$ relates the currents and voltages at the feed ports with edge ports open. Again, we use the three-dimensional analysis to obtain this sub-matrix. The electric current is calculated from the H-field.

$[H_{22}]$ relates the currents at the feed ports due to impressed currents at the edge ports with the feed ports shorted. Two-dimensional analysis is applicable to this computation also. However, it can be shown (see Appendix C) that this sub-matrix is the negative transpose of $[H_{11}]$.

The Z-matrix for the PAN can be computed from the hybrid matrix by using the equations given below:

$$\begin{bmatrix} \hat{V}_E \\ \hat{V}_F \end{bmatrix} = \begin{bmatrix} [Z_{EE}][Z_{EF}] \\ [Z_{FE}][Z_{FF}] \end{bmatrix} \begin{bmatrix} \hat{I}_E \\ \hat{I}_F \end{bmatrix} \qquad (3.30)$$

where

$$[Z_{FF}] = [H_{21}^{-1}] \qquad (3.30a)$$

$$[Z_{FE}] = [-H_{21}^{-1}]\,[H_{22}] \tag{3.30b}$$

$$[Z_{EF}] = [H_{11}]\,[-H_{21}^{-1}] \tag{3.30c}$$

$$[Z_{EE}] = [H_{12}] - [H_{11}]\,[H_{21}^{-1}]\,[H_{22}] \tag{3.30d}$$

The procedures for obtaining the Z-matrix for both the Feed Network and the Edge-Admittance Network have been discussed in Chapter 2.

3.7 Segmentation and Far-Field Calculations

Once the Z-matrices of the Feed Network, Patch Network and the Edge-Admittance Network are computed, they are combined to yield the overall 1x1 impedance matrix of the radiating structure (see Figure 2.11). The procedure of combining the Z-matrices of sub-networks into a matrix for the connected network is known as segmentation [8]. In implementing this technique, we first combine the FLN with the PAN. The resulting network is then connected to the EAN and the overall network representation of the radiating configuration is obtained. The segmentation method also yields the voltages at the edge ports so that the radiation field of this configuration can be calculated. The radiation vector is given by [1], [7]

$$\vec{L} = -2 \sum_{n}^{N_P} \vec{a}_t W_n V_n e^{jk_0 \rho_n \sin\theta \cos(\phi - \phi_0)} \tag{3.31}$$

where W_n and V_n are the width and voltage, respectively, at the n_{th} edge port.

The radiation E-field components are then given by (refer to Figure 3.4 for the coordinate orientation)

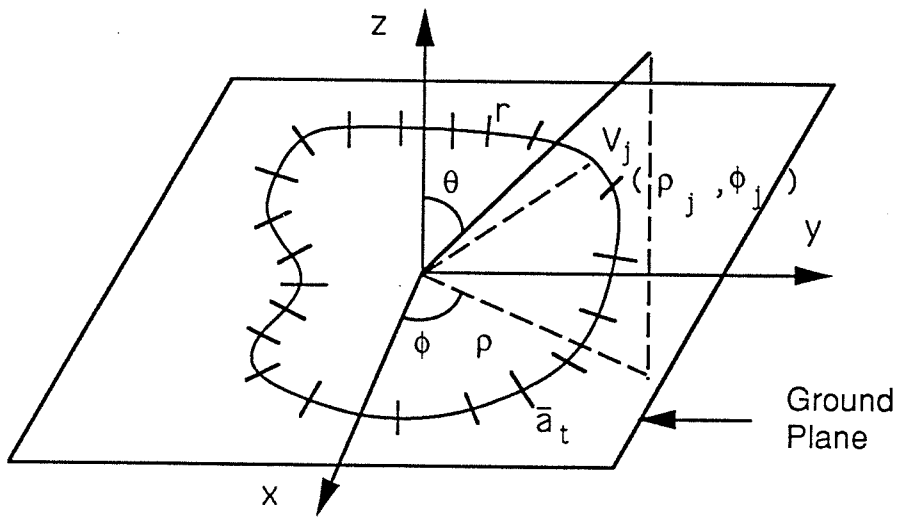

Figure 3.4: Equivalent magnetic current line source for a microstrip patch on thin substrate

$$E_\theta = -j\frac{\vec{L}\cdot\vec{a_\phi}}{2\lambda_0 r}\, e^{-jk_0 l} \qquad (3.32)$$

and

$$E_\phi = j\frac{\vec{L}\cdot\vec{a_\theta}}{2\lambda_0 r}\, e^{-jk_0 l} \qquad (3.33)$$

CHAPTER 4

NUMERICAL RESULTS

In this chapter, we present numerical results obtained from the model developed for two-layer patch antenna systems. Results for both monolithic as well as hybrid configurations are given. Comparison of some of these results with the full-wave analysis code PMESH are also presented.

The parameters of prime interest to the antenna designer are the input impedance of the antenna, frequency bandwidth of its operation and its radiation pattern. A sample monolithic case is shown in Figure 4.1.

Case 1:

In this case, the heights h_1 and h_2 are taken to be 10 mils and 100 mils, respectively. The dielectric constants of the two layers are kept equal with $\varepsilon_1=\varepsilon_2=2.2$.

In Figure 4.2a, the variation of input impedance (input impedance is referenced to the XX plane) and comparison of the MNM and PMESH results are shown on the Smith Chart. These results are also plotted on a linear scale in Figure 4.2b. The far-field radiation pattern for E_ϕ is shown in Figure 4.2c.

Case 2:

In this case, we keep the height and the dielectric constants of the two layers equal. That is, $h_1 = h_2 = 1.58$ mm and $\varepsilon_1 = \varepsilon_2 = 2.2$. The variation of input impedance and comparison with PMESH are shown in Figures 4.3a and 4.3b.

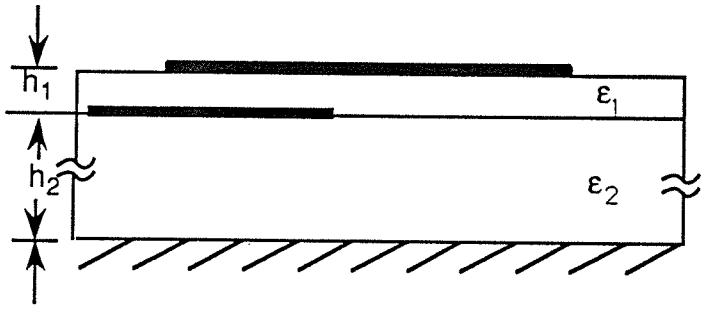

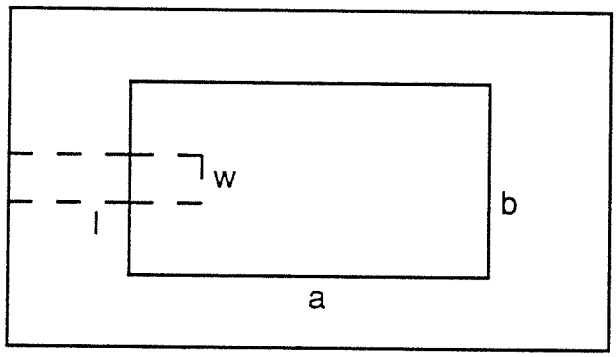

a = 2.5 cms

b = 4 cms

l = 1.25 cms

w = 0.5 cms

Figure 4.1: A monolithic configuration

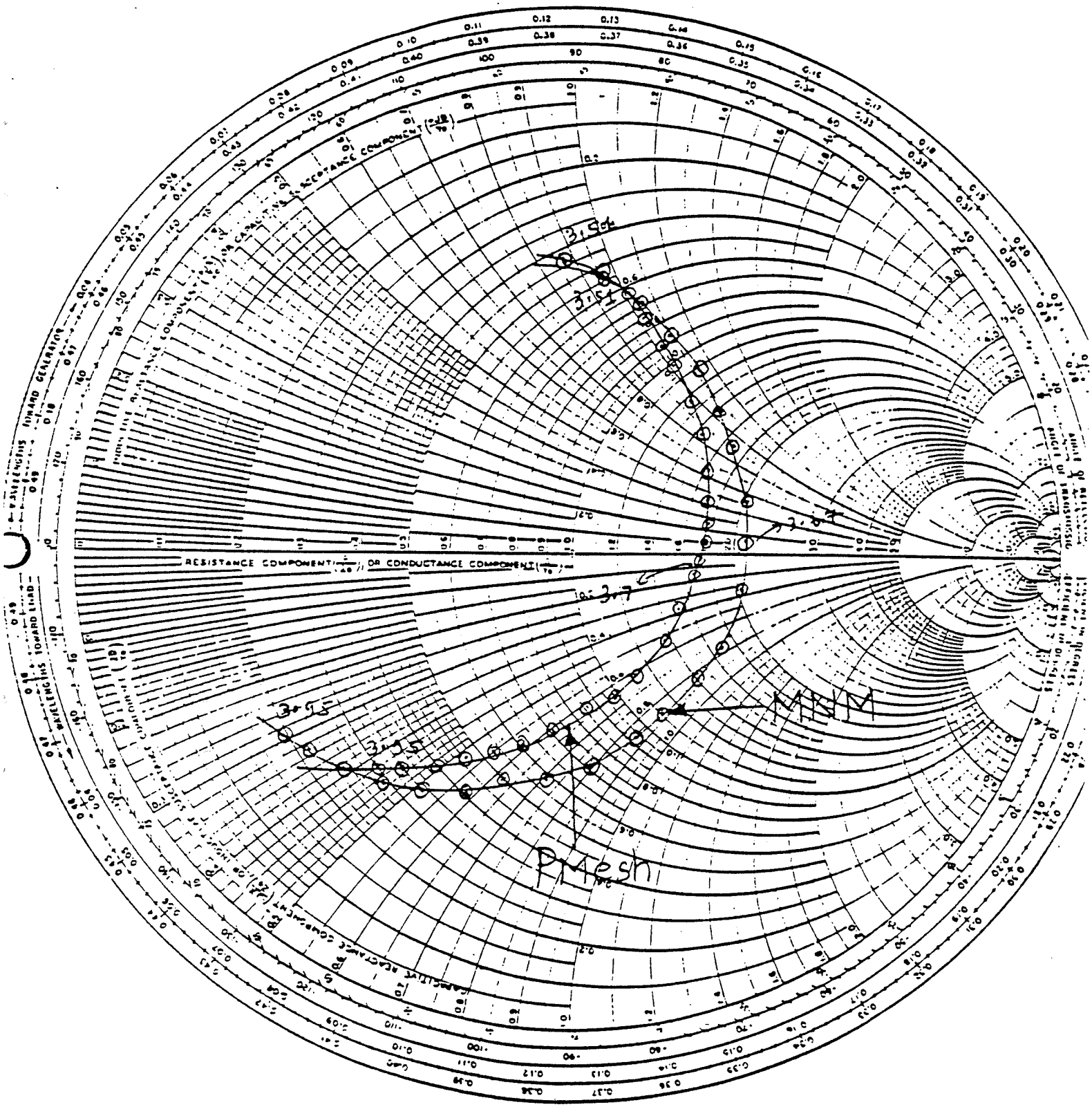

Figure 4.2a: Case 1 - Input Impedance on the Smith Chart

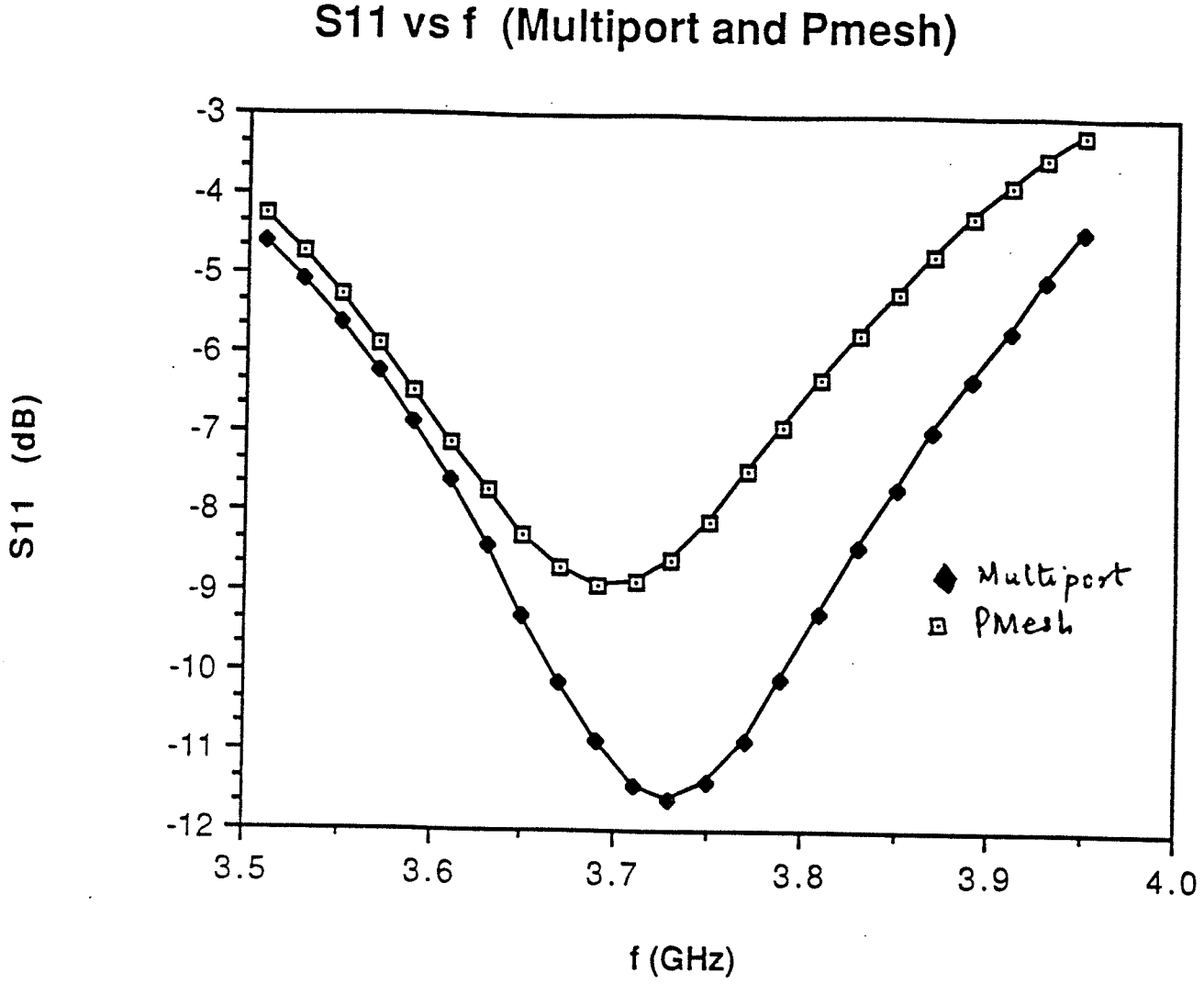

Figure 4.2b: Case 1 - Input Impedance on a Linear Scale.

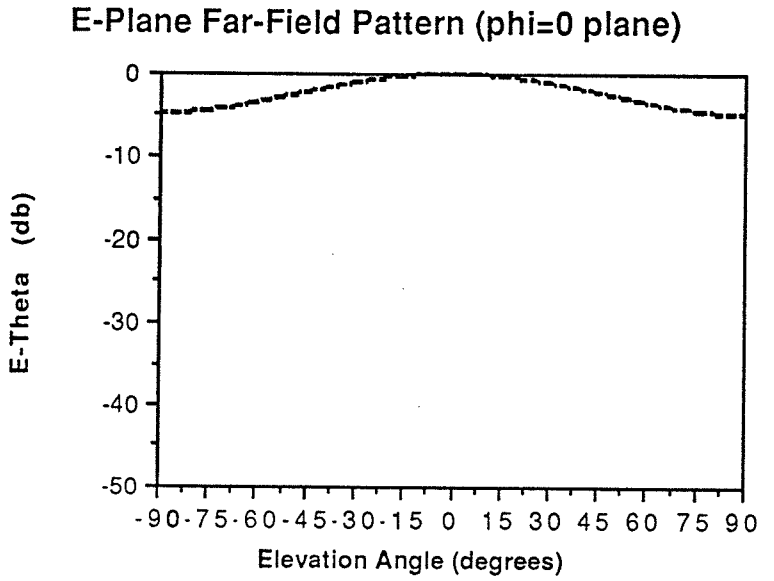

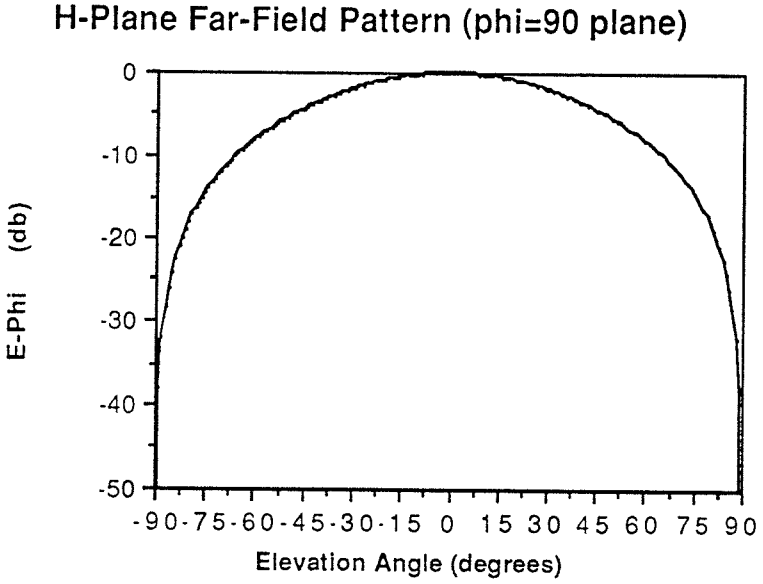

Figure 4.2c: Far Field Pattern

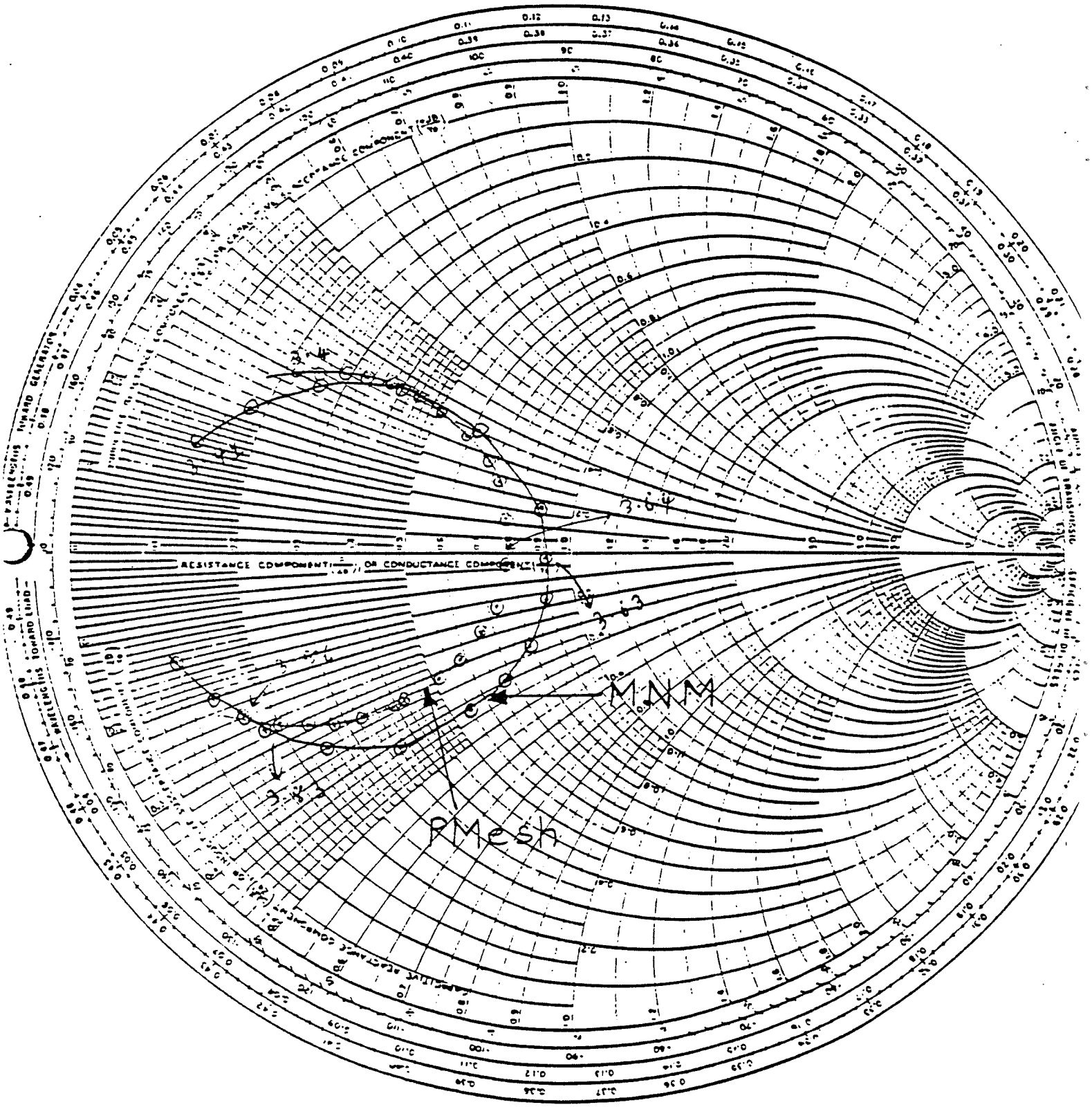

Figure 4.3a: Case 2 - Input Impedance on the Smith Chart.

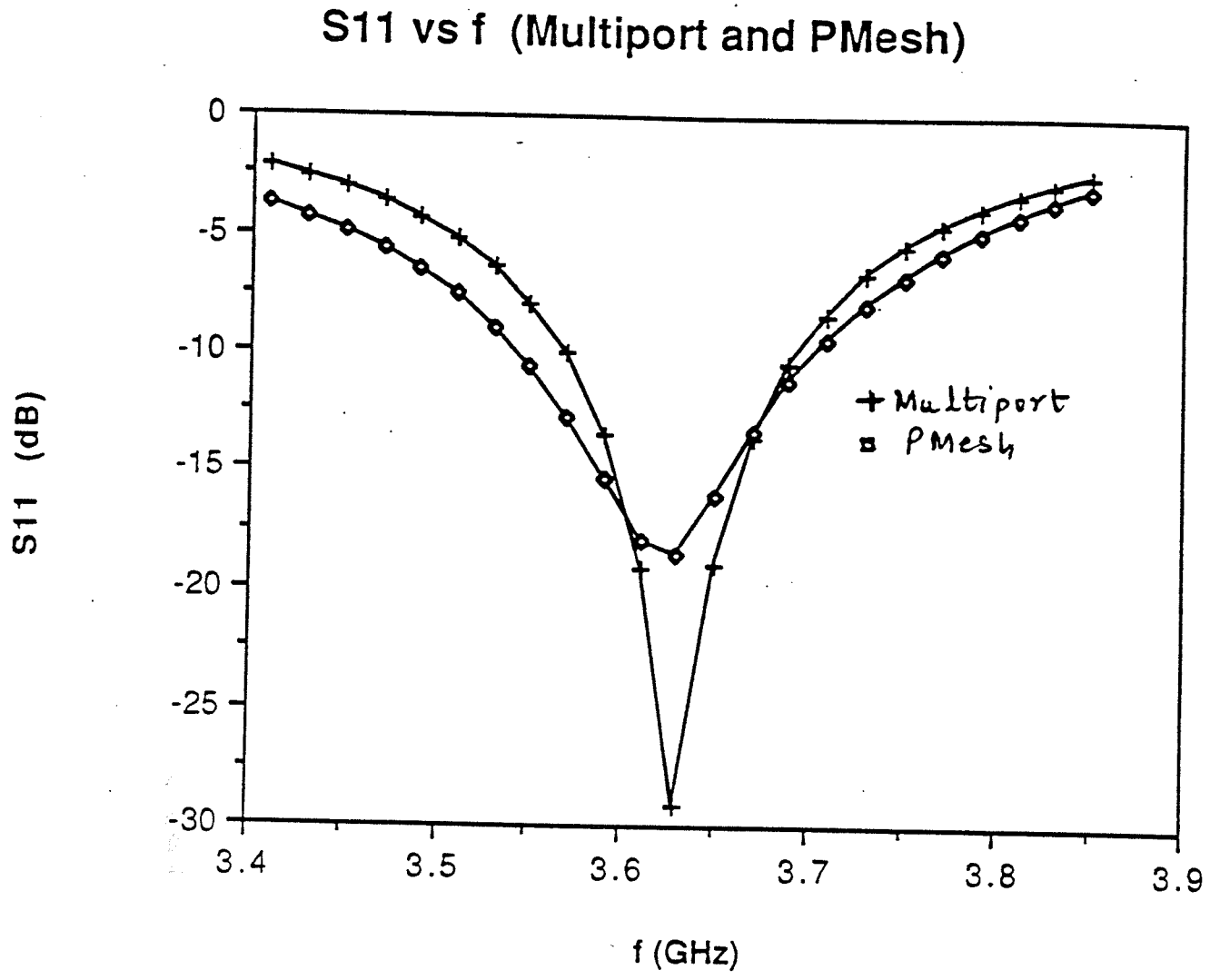

Figure 4.3b: Case 2 - Input Impedance on a Linear Scale.

Case 3:

This is a realistic simulation of the monolithic case and the dimensions are: $h_1 = 10$ mils, $h_2 = 100$ mils, $\varepsilon_1 = 2.2$ and $\varepsilon_2 = 10.5$. Results of the input impedance are shown in Figure 4.4a.

The field in the open cavity is calculated by summing over an infinite number of modes. In practice, this operation is truncated after summing over a finite number of modes. This number is determined after examining the convergence of the field. In Figure 4.4b, a graph, showing the convergence of the input impedance as a function of the mode number for Case 3, is presented. The mode number indicates the upper limit of the sum of the modes in the x, y and z directions.

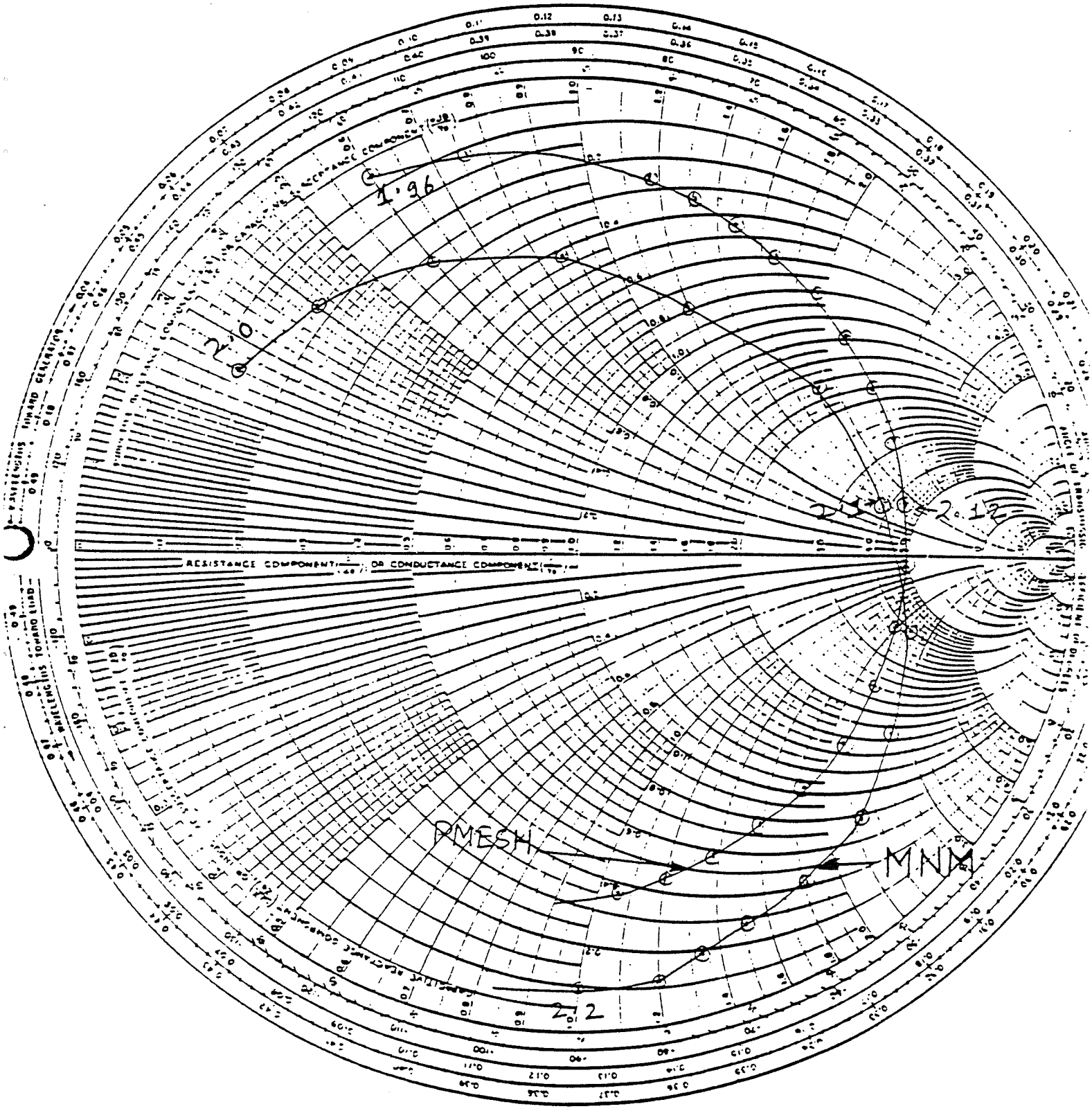

Figure 4.4a: Case 3 - Input Impedance on the Smith Chart.

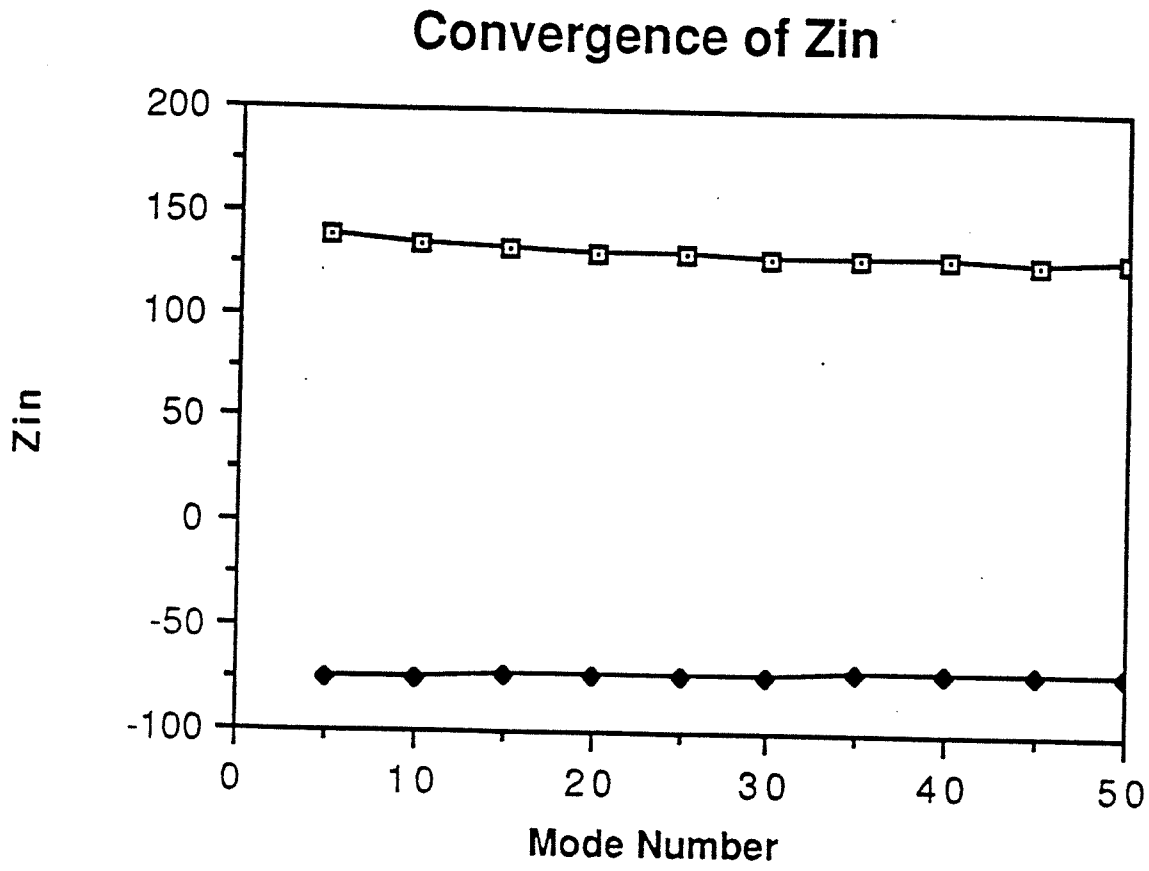

Figure 4.4b: Convergence Results.

CHAPTER 5

CONCLUDING REMARKS AND DISCUSSION

In the preceding chapters, we have presented the development of a model for two-layer microstrip patch antennas suitable for integration in monolithic and hybrid circuit configurations and the analytical treatment required in its implementation. The model is based on the MNM technique which transforms an electromagnetic field problem into a circuit problem. Some sample results have been presented and compared with the full-wave analysis solver PMESH. The MNM approach had several advantages; the technique is relatively easy to implement, computationally far less expensive than existing full-wave numerical methods and provides valuable physical insight into the operation of the antenna.

5.1 Suggestion for Refinements in Current Model

The philosophy adopted in our research is that the developed model should be essentially simple and at the same time yield itself to workable designs. In this section, we discuss some issues, dealing with refining the current model, which became apparent during the course of this work. These modifications are likely to lead to a more accurate model.

Consider the monolithic configuration shown in Figure 5.1. The Schelkunoff surface which separates the 'source' region from the 'field' region is shown in Figure 5.1. The Love's Equivalence Theorem [17] (a version of the Schelkunoff Equivalence Theorem) is applied to the Schelkunoff surface of Figure 5.1. Since surface to the right of XX coincides with the conducting patch the tangential electric field on it vanishes. Hence, the equivalent magnetic current on this surface is zero. The equivalent electric current is effectively

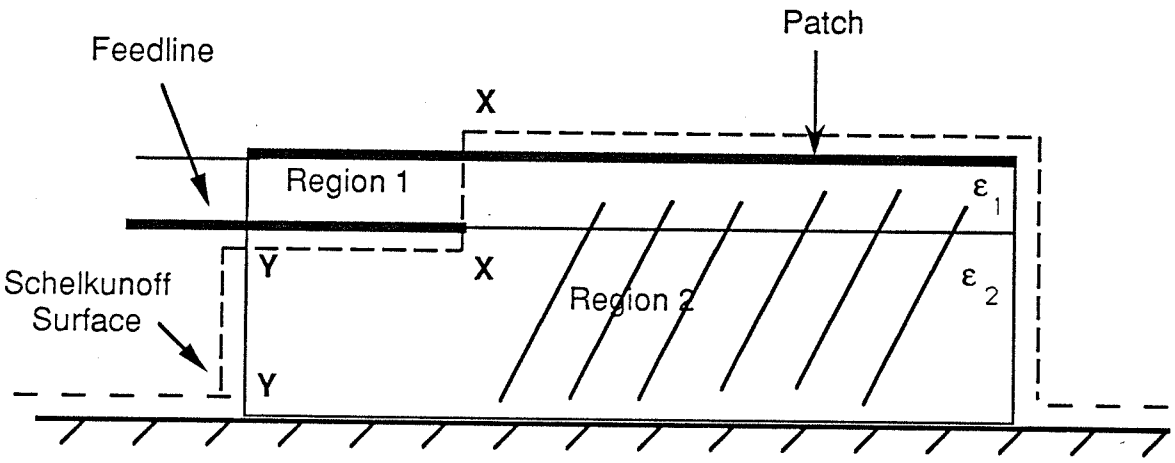

Figure 5.1: Separation of the Source Region by Application of Schelkunoff Theorem

cancelled due to the conducting material backing the said surface (Love's Theorem). On the surface denoted by XX, a tangential component of electric field is present and hence equivalent magnetic current elements are placed at the periphery of the feed structure. The surface XY coincides with the conductor of the feedline and hence the equivalent magnetic current is zero in this region. There are also electric field lines from the feedline to the ground plane giving rise to another source which contributes to the patch excitation; this source has been neglected in the current model. In order to model the excitation accurately, this contribution needs to be taken into account. For that purpose, equivalent electric current elements are placed at the interface (YY in Figure 5.1). The equivalent electric and magnetic current sources exciting the patch are shown in Figure 5.2. The circuit model of the Feed Network (FN) in this case is as shown in Figure 5.3 where EFN models the portion of feedline outside the patch. Ports F_e are connected to the output ports of the EFN to model the excitation by equivalent electric currents at the interface YY (Figure 5.1). Ports F_m model the excitation by equivalent magnetic currents at interface XX as considered in the analysis presented in this report. Inclusion of the excitation via ports F_e is likely to lead to a more accurate model.

5.2 Further Work

The investigations reported here need to be extended in the following respects.

a) Incorporation of the Generalized Radiation Conductance Network (GRCN) into the Edge-Admittance Network. As was mentioned in Chapter 2, the expressions for the radiation conductance in the current model are valid only if the voltage distribution along the edges of the patch is known *a priori*. This constraint is removed by using the GRCN developed recently.

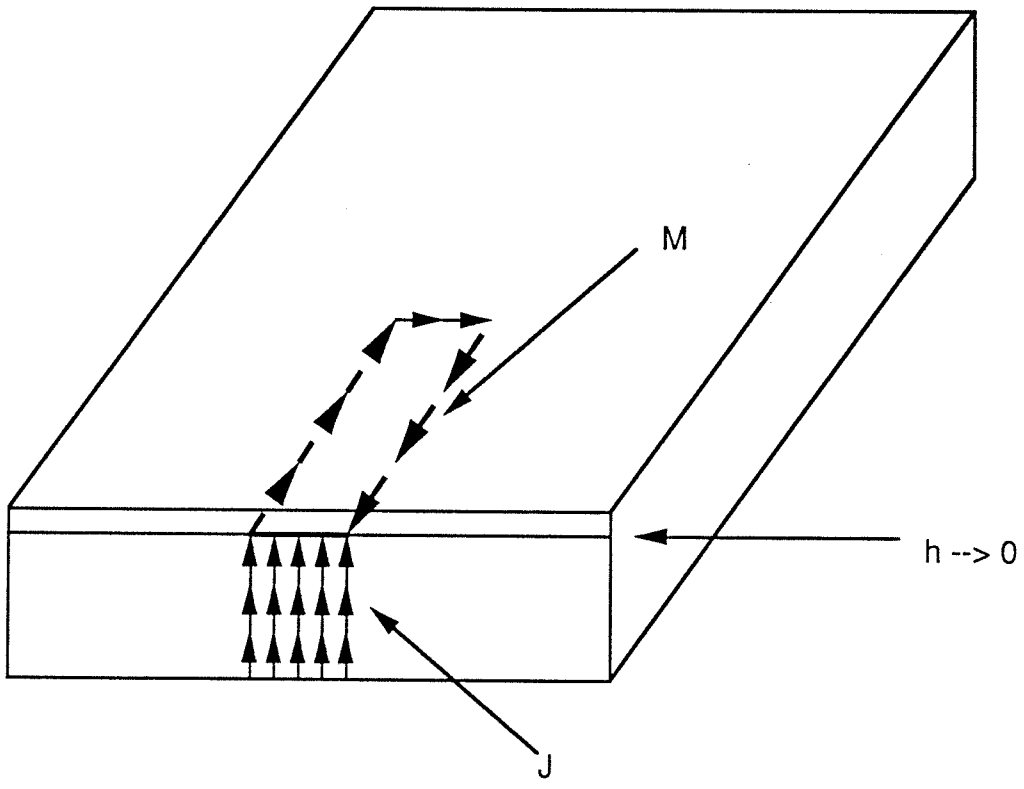

Figure 5.2: Equivalent Electric and Magnetic Current Sources
Due to Feedline Exciitation

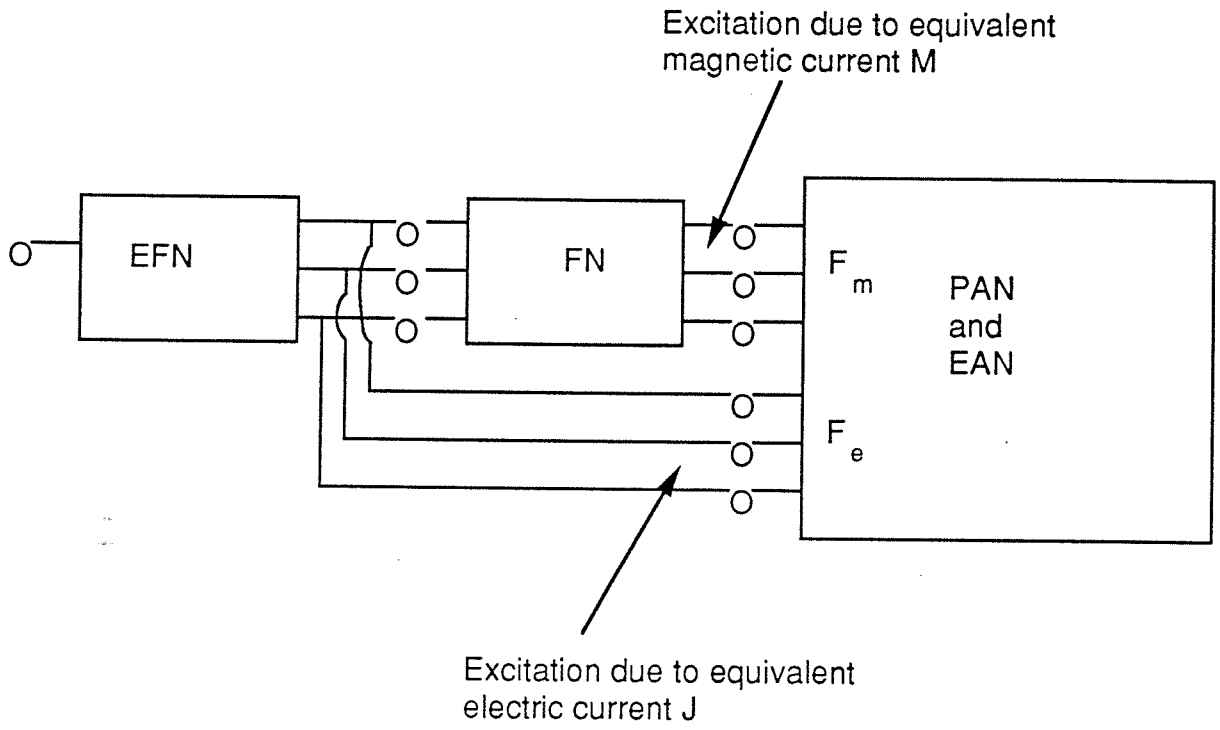

Figure 5.3: Schematic diagram of the Overall Feed Network

b) Parametric study of the width of the feedline needs to be carried out. This will enable us to evaluate the variation of the input impedance of the antenna with the width of the feedline.

c) As mentioned in Chapter 1, there is a possibility of increasing the antenna bandwidth by using a feeder patch on the lower layer in hybrid configurations. This needs to be explored.

d) A quantitative comparison of computation time of the current model developed and the full-wave code PMESH is also desirable.

The research presented in this report has dealt with passive feed structures. The modeling and analysis approach is also applicable to the case when active devices are used to excite the patch. In future, we intend investigating feed structures using active devices such as Gunn diodes.

LIST OF REFERENCES

[1] James, J. R., Hall, P. S., Wood, C., *Microstrip Antenna Theory and Design*, Peter Peregrinus Ltd., 1981.

[2] Karmarkar, N.C., Bhattacharyya, A., 'Electromagnetically Coupled Patch Antenna - Theoretical and Experimental Investigations', Microwave and Optical technology Letters, vol 5, No 3, March 1992, pp 115-118.

[3] Karmarkar, N.C., Bialkowski, M. E., 'Experimental Investigations into an Electromagnetically Coupled Microstrip Patch Antenna', Microwave and Optical technology Letters, vol 5, No 9, August 1992, pp 447-453.

[4] Pozar, D., Kaufman, B., 'Increasing the Bandwidth of a Microstrip Antenna by Proximity Coupling', Electronics Letters, vol 23, No 8, pp 368-369, April 1987.

[5] Pozar, D., Voda, S., 'A Rigorous Analysis of a Microstrip Line Fed Patch Antenna', IEEE Transactions on Antennas and Propagation, vol 35, No 12, pp 1343-1349, December 1987.

[6] Gupta, K. C., 'Computer-Aided Design of Microstip Antennas and Arrays', Fall 1991 Course Notes, ECE Dept, University of Colorado at Boulder.

[7] Benalla, A., Gupta, K. C., 'Design Procedure for Linear Series-Fed Arrays of Microstrip Patches Covered with a Thick Dielectric Layer', Scientific Report No. 100, 1989, Electromagnetics Laboratory, ECE Dept., University of Colorado at Boulder.

[8] Gupta, K. C., Garg, R., Chadha, R., *Computer-Aided Design of Microwave Circuits*, Artech House, 1981.

[9] Benalla, A., Gupta, K. C., 'Multiport Network Model and Transmission Characteristics of Two-Port Rectangular Microstrip Patch Antennas', IEEE

Transactions on Antennas and Propagation, Vol 36, pp 1337-1342, October 1988.

[10] Lee, H., Tripathi, V. K., 'Generalized Spectral Domain Analysis of Planar Structures Having Semi-Infinite Ground Planes', IEEE MTT-S, International Microwave Symposium Digest, pp327-329, 1984.

[11] Kollipara, R. T., Tripathi, V. K., 'Quasi-TEM Spectral Domain Technique for Multiconductor Structures with Rectangular and Trapezoidal Conductor Cross-Section', Microwave and Optical Technolofy Letters, vol 3, No 1, January 1990.

[12] Crampagne, R., Ahmadpanah, M., Guiraud, J., 'A Simple Method for Determining the Green's Function for a Large Class of MIC Lines Having Multilayered Dielectric Structures', IEEE Transactions on Microwave Theory and Techniques, vol 26, No 2, pp 82-87, February 1978.

[13] Okoshi, T., *Planar Circuits for Microwaves and Lightwaves*, Springer-Verlag, 1985.

[14] Hammerstad, E. O., 'Equations for Microstrip Circuit Design', 5th European Microwave Conference, pp268-272, September 1975.

[15] Benalla, A., Gupta, K. C., 'Generalized Edge-Admittance Network for Modeling of Radiation from Microstrip Patch Antennas', National Radio Science Meeting, January 7-10, 1992, Boulder, Colorado.

[16] Harrington, R., *Time Harmonic Electromagnetic Fields*, McGraw Hill, 1961.

[17] Balanis, C., *Advanced Engineering Electromagnetics*, John Wiley and Sons, 1989.

[18] Johnson, C. C., *Field and Wave Electrodynamics*, McGraw Hill, 1965.

[19] Collins, R., *Field Theory of Guided Waves*, IEEE Press, 1991.

APPENDIX A

COMPARISON OF TWO-LAYER CAVITY RESONANCE FREQUENCIES OBTAINED BY TRANSCENDENTAL EQUATION AND BY EFFECTIVE DIELECTRIC CONSTANT METHOD

Consider the two-layer open cavity as shown in Figure A1. The solution for the source-free fields in this cavity is split into the TE_z and TM_z modes. The continuity of the tangential electric and magnetic fields at the interface of the two layers leads to a characteristic equation [17]. This characteristic equation is of the transcendental type and its solution leads to the resonance frequencies of the cavity.

Let $\alpha_1 = m\pi/a$, $\alpha_2 = n\pi/b$ (m, n =0, 1, 2, ...) and β_{z1}, β_{z2} be the wavenumbers in the z-direction in layers 1 and 2, respectively. Then, the characteristic equations are[]:

For TE modes,

$$\frac{\tan[\beta_{z1} h_1]}{\beta_{z1}} = -\frac{\tan[\beta_{z2} h_2]}{\beta_{z2}} \qquad \text{(A1)}$$

For TM modes,

$$\frac{\beta_{z1} \tan[\beta_{z1} h_1]}{\varepsilon_1} = -\frac{\beta_{z2} \tan[\beta_{z2} h_2]}{\varepsilon_2} \qquad \text{(A2)}$$

In deriving equations (A1) and (A2), the implicit assumtion is that $\mu_1 = \mu_2 = \mu_0$. The wavenumbers are related to the resonance frequencies (ω) by the following equations:

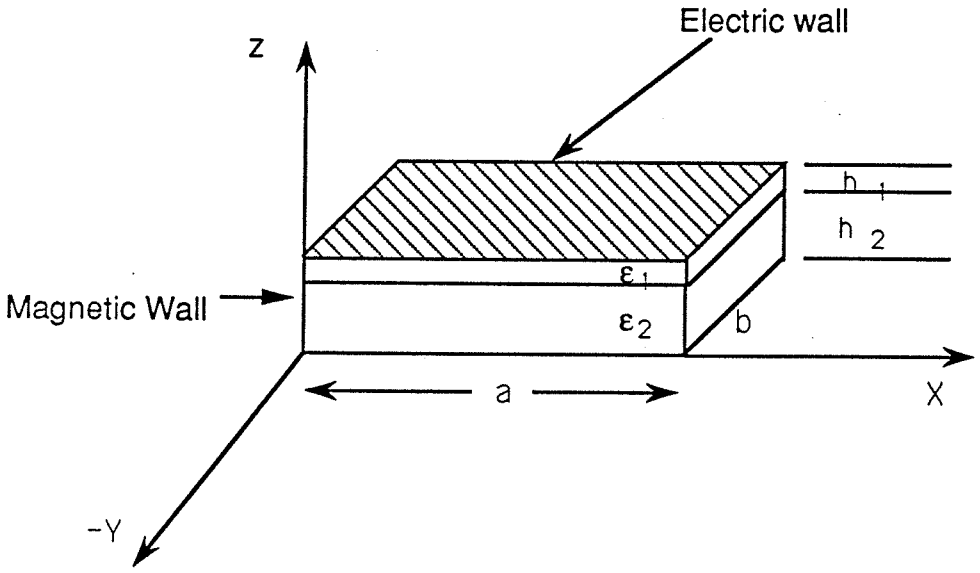

Figure A1: Two-layer open cavity

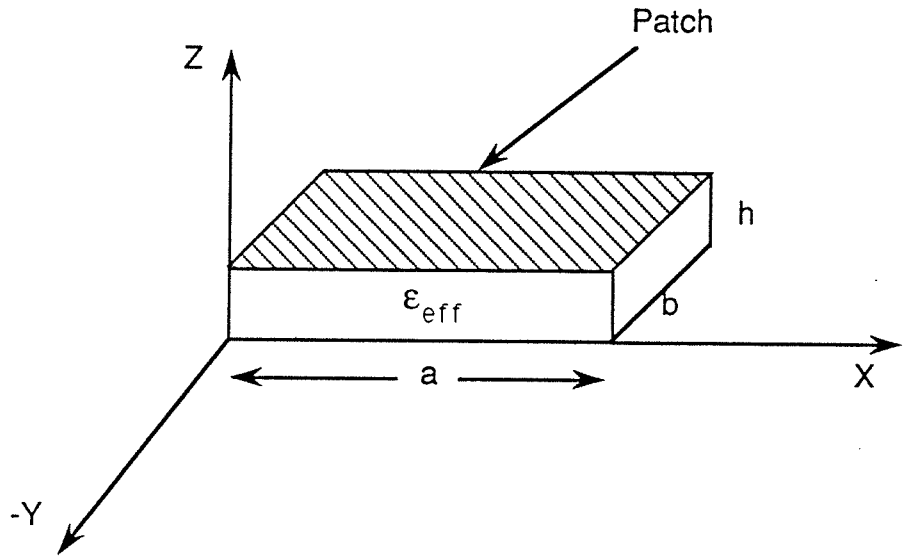

Figure A2: Single layer open cavity with effective dielectric constant

$$(\alpha_1)^2 + (\alpha_2)^2 + (\beta_{z1})^2 = \omega^2 \varepsilon_1 \mu_0 \qquad \text{(A3)}$$

$$(\alpha_1)^2 + (\alpha_2)^2 + (\beta_{z2})^2 = \omega^2 \varepsilon_2 \mu_0 \qquad \text{(A4)}$$

where α_1, α_2 are given along with equation (3.3).

Equations (A3) and (A4) are used in (A1) and (A2) to solve for the resonance frequencies.

The computation of the resonance frequencies by the above approach is cumbersome since it entails solving the transcendental equation associated with each mode. Considerbable simplification is brought about by defining an effective dielectric constant wherein the two-layer cavity is converted into a homogenously filled one shown in Figure A2. Using the equivalence of capacitances, the cavity in Figure A1 is considered as a combination of two parallel plate capacitors in series (of heights h_1 and h_2). The effective dielectric constant is extracted from the equivalent capacitance. This procedure yields:

$$\varepsilon_{eff} = \frac{\varepsilon_1 \varepsilon_2 (h_1 + h_2)}{\varepsilon_1 h_2 + \varepsilon_2 h_1} \qquad \text{(A5)}$$

The resonance frequencies are calculated using

$$\omega = \sqrt{\frac{(\alpha_1)^2 + (\alpha_2)^2 + (\alpha_3)^2}{\mu_0 \varepsilon_{eff}}} \qquad \text{(A6)}$$

where $\alpha_3 = p\pi/h$ and α_1 , α_2 are as defined earlier (p=0,1,2... and $h = h_1+h_2$).

Table 1 lists a comparison of the resonance frequencies of the cavity calculated by two methods described above. The first method utilises the concept of effective dielectric constant. In the second approach, the transcendental

equation for the resonant frequencies of a two-layer cavity is solved. It can be seen that the use of the effective dielectric constant yields results with far less computation time and without sacrificing accuracy.

TABLE 1

Mode			f_r(eff) GHz	f_r(trans)GHz	%error
m	n	p			
1	0	0	8.383650	8.383650	$<10^{-6}$
0	1	0	13.972751	13.972749	1.4×10^{-5}
1	1	0	16.294888	16.294885	1.84×10^{-7}
2	0	0	16.767301	16.767298	1.78×10^{-7}
2	1	0	21.826135	21.826128	3.20×10^{-7}
1	2	0	29.175961	21.175945	5.48×10^{-7}
2	2	0	32.589780	32.589753	8.28×10^{-7}

f_r(eff) - resonant frequency calculated from effective dielectric constant

f_r(trans) - resonant frequency calculated from transcendental equation

m,n,p - mde numbers for the x,y and z directions, respectively

The parameters of the cavity are:

$a = 0.5$ cms, $b = 0.3$ cms, $h_1 = 1$ micron, $h_2 = 100$ microns

$\varepsilon_1 = 7.0$, $\varepsilon_2 = 12.9$

APPENDIX B

CALCULATION OF TE_Z AND TM_Z MODE FIELDS

The electromagnetic fields in an open cavity satisfy Maxwell's equation subject to the boundary conditions at the walls of the cavity. However, in practice, it is convenient to define the auxiliary potentials **F**, the electric vector potential and **A**, the magnetic vector potential, to compute the fields. Mathematically, these potentials are defined as [17]

$$\nabla \times \mathbf{F} = -\varepsilon \mathbf{E} \qquad \text{(B1)}$$

$$\nabla \times \mathbf{A} = \mu \mathbf{E} \qquad \text{(B2)}$$

The fields in the cavity are obtained by choosing suitable combination of the vector potentials **A** and **F**. To obtain the the TE_z field, we choose,

$$\mathbf{A} = 0 \qquad \text{(B3.a)}$$

$$\mathbf{F} = \mathbf{a}_z F_z (x,y,z) \qquad \text{(B3.b)}$$

with

$$F_z = A_{mnp} \sin \alpha_1 x \sin \alpha_2 y \sin \alpha_3 z \qquad \text{(B4)}$$

where $\alpha_1 = m\pi/a$, $\alpha_2 = n\pi/b$ and $\alpha_3 = p\pi/h$ (see Figure 2.4 for the cavity parameters). The actual field components are obtained from the following set of equations [13]:

$$E_x = -\frac{1}{\varepsilon}\frac{\delta F_z}{\delta y}$$

$$E_y = -\frac{1}{\varepsilon}\frac{\delta F_z}{\delta z}$$

$$E_z = 0$$

$$H_x = -j\frac{1}{\omega\mu\varepsilon}\frac{\delta^2 F_z}{\delta x\,\delta z}$$

$$H_y = -j\frac{1}{\omega\mu\varepsilon}\frac{\delta^2 F_z}{\delta y\,\delta z}$$

$$H_z = -j\frac{1}{\omega\mu\varepsilon}\left(\frac{\delta^2}{\delta z^2} + \beta^2\right)F_z$$

Similarly, to get the TM_z field, we set

$$\mathbf{F} = 0 \qquad \text{(B6.a)}$$

$$\mathbf{A} = \mathbf{a}_z A_z(x,y,z) \qquad \text{(B6.b)}$$

with

$$A_z = B_{mnp}\cos\alpha_1 x \cos\alpha_2 y \cos\alpha_3 z \qquad \text{(B7)}$$

The field compnents are given by:

$$E_x = -j \frac{1}{\omega\mu\varepsilon} \frac{\delta^2 A_z}{\delta x \, \delta z}$$

$$E_y = -j \frac{1}{\omega\mu\varepsilon} \frac{\delta^2 A_z}{\delta y \, \delta z}$$

$$E_z = -j \frac{1}{\omega\mu\varepsilon} \left(\frac{\delta^2}{\delta z^2} + \beta^2 \right) A_z$$

$$H_x = -\frac{1}{\mu} \frac{\delta A_z}{\delta y}$$

$$H_y = -\frac{1}{\mu} \frac{\delta A_z}{\delta x}$$

$$H_z = 0$$

APPENDIX C

EVALUATION OF THE SUB-MATRIX $[H_{22}]$

It has been pointed out in Chapter 3 that the sub-matrix $[H_{22}]$ is the negative transpose of the sub-matrix $[H_{11}]$. The proof of that assertion is provided in this Appendix.

Equations (3.30), on which the proof is based, are reproduced below. Equation (3.30) relates the edge and feed voltages to the edge and feed currents via a Z-matrix while equations (3.30a) through (3.30d) relate the submatrices of the Z-matrix to the components of the intermediate hybrid matrix.

$$\begin{bmatrix} \widehat{V_E} \\ \widehat{V_F} \end{bmatrix} = \begin{bmatrix} [Z_{EE}][Z_{EF}] \\ [Z_{FE}][Z_{FF}] \end{bmatrix} \begin{bmatrix} \widehat{I_E} \\ \widehat{I_F} \end{bmatrix} \tag{3.30}$$

where

$$[Z_{FF}] = \left[H_{21}^{-1}\right] \tag{3.30a}$$

$$[Z_{FE}] = \left[-H_{21}^{-1}\right] [H_{22}] \tag{3.30b}$$

$$[Z_{EF}] = [H_{11}] \left[-H_{21}^{-1}\right] \tag{3.30c}$$

$$[Z_{EE}] = [H_{12}] - [H_{11}] \left[H_{21}^{-1}\right] [H_{22}] \tag{3.30d}$$

The impedance matrix of a passive network is reciprocal. Hence the submatrices, $[Z_{FE}]$ in equation (3.30b) and $[Z_{EF}]$ in equation (3.30c), must be the transpose of one another. Therefore,

$$\left[H_{21}^{-1}\right]\left[H_{22}\right] = \left(-\left[H_{11}\right]\left[H_{21}^{-1}\right]\right)^{t} \qquad \text{(C1)}$$

where the superscript 't' indicates the transpose operator. Using the property of the transpose operator, the right-hand side in (C1) becomes

$$\left[H_{21}^{-1}\right]\left[H_{22}\right] = -\left[H_{21}^{-1}\right]^{t}\left[H_{11}\right]^{t} \qquad \text{(C2)}$$

$[H_{21}]$ represents an admittance matrix and hence its inverse and the transpose of its inverse are equal. Given this information, equation (C2) reduces to

$$\left[H_{22}\right] = -\left[H_{11}\right]^{t} \qquad \text{(C3)}$$